JCTC Journal of Chemical Theory and Computation

pubs.acs.org/JCTC Article

Nonadiabatic Dynamics with Exact Factorization: Implementation and Assessment

Daeho Han and Alexey V. Akimov*

Cite This: J. Chem. Theory Comput. 2024, 20, 5022−5042 Read Online

ACCESS | Metrics & More | Article Recommendations | Supporting Information

ABSTRACT: In this work, we report our implementation of several independent-trajectory mixed-quantum-classical (ITMQC) nonadiabatic dynamics methods based on exact factorization (XF) in the Libra package for nonadiabatic and excited-state dynamics. Namely, the exact factorization surface hopping (SHXF), mixed quantum-classical dynamics (MQCXF), and mean-field (MFXF) are introduced. Performance of these methods is compared to that of several traditional surface hopping schemes, such as the fewest-switches surface hopping (FSSH), branching-corrected surface hopping (BCSH), and the simplified decay of mixing (SDM), as well as conventional Ehrenfest (mean-field, MF) method. Based on a comprehensive set of 1D model Hamiltonians, we find the ranking SHXF ≈ MQCXF > BCSH > SDM > FSSH ≫ MF, with the BCSH sometimes outperforming the XF methods in terms of describing coherences. Although the MFXF method can yield reasonable populations and coherences for some cases, it does not conserve the total energy and is therefore not recommended. We also find that the branching correction for auxiliary trajectories is important for the XF methods to yield accurate populations and coherences. However, the branching correction can worsen the quality of the energy conservation in the MQCXF. Finally, we find that using the time-dependent Gaussian width approximation used in the XF methods for computing decoherence correction can improve the quality of energy conservation in the MQCXF dynamics. The parameter-free scheme of Subotnik for computing the Gaussian widths is found to deliver the best performance in situations where such widths are not known a priori.

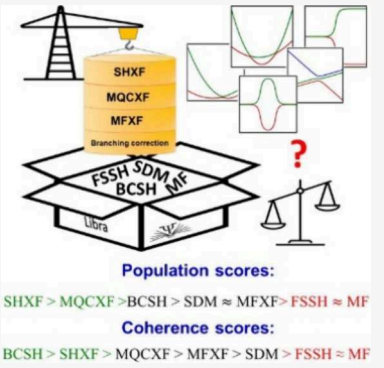

1. INTRODUCTION

With the rising demand for simulating and predicting a variety of chemical reactions and excited-state phenomena in photosynthetic systems,[1−3] organic semiconductors,[4,5] and photocatalysts,[6,7] and so forth, the importance of developing accurate yet efficient nonadiabatic (NA) dynamics algorithms cannot be overemphasized. In this context, a multitude of mixed quantum-classical methods[8−14] has been developed and widely employed. They enable modeling of a correlated dynamics of electrons and nuclei while treating them as quantum and classical particles, respectively.[15] Resorting to classical trajectories, the nuclear evolution is as simple as propagating classical degrees of freedom and the necessary amount of electronic information can be restricted along the corresponding classical sampling. One of the most successful examples of applying this scheme is the trajectory-based surface hopping (SH) method, where the electronic transitions are handled through discrete jumps between adiabatic potential energy surfaces computed on demand in each time step.[16−18]

Dealing with the correlated dynamics of electrons and nuclei and capturing the electronic coherence and decoherence correctly are all essential aims. However, they are missing in the traditional algorithms such as Ehrenfest[19] or Tully's fewest-switches SH (FSSH)[18] methods. For this purpose, a plethora of decoherence algorithms has been developed. Some decoherence algorithms, such as coherent switching with decay of mixing (CSDM),[20] simplified decay of mixing (SDM),[21] or its modified version (mSDM),[22] utilize a decoherence time parameter to provide a correction to the electronic equation. This parameter can be estimated in a variety of ways,[23] by using energy gap magnitudes[9,21,24,25] and their variations,[26,27] as well as the force and momenta differences for particle propagating on different electronic potential energy surfaces. Furthermore, starting from wave function overlaps, this decoherence time can be described within a Gaussian approximation as in the works of Truhlar et al.,[26] Schwartz et al.,[27] and Subotnik et al.[28,29] Alternatively, one can use the optical response function formalism of Mukamel[30] or a related approach based on the energy gap autocorrelation function used in many works of the Prezhdo group.[10,31,32] Also, the multiple-spawning approach takes another category, explaining the interaction between nuclear wave packets directly with a swarm of classical trajectories.[33,34]

Received: March 18, 2024
Revised: May 8, 2024
Accepted: May 9, 2024
Published: June 5, 2024

https://doi.org/10.1021/acs.jctc.4c00343
J. Chem. Theory Comput. 2024, 20, 5022−5042

Among a variety of decoherence algorithms, decoherence-corrected NA dynamics methods based on exact factorization (XF) have proven useful.[35−37] XF serves as a rigorous starting point for describing coupled motion of electrons and nuclei, where a molecular wave function is factored into the nuclear component and the conditional electronic wave function.[38] The mixed quantum-classical approach can be applied to XF, resulting in the coupled-trajectory mixed quantum-classical (CTMQC) scheme.[39,40] Compared to the conventional approach, explicit decoherence due to electron−nuclear coupling naturally emerges in the corresponding time-dependent Schrodinger equation (TD-SE) in the CTMQC method. The decoherence correction takes the form of an electron−nuclear coupling explicitly defined by the quantum momentum and time-dependent vector potential. Recent works have addressed various aspects of the CTMQC method such as computing the quantum momentum,[41] improving the energy conservation,[42−44] and introducing simplified nuclear propagation schemes motivated by the surface hopping.[45]

Compared to CTMQC, independent-trajectory mixed quantum-classical (ITMQC) methods based on XF offer notable advantages in terms of computational cost and robustness to failures of individual trajectories. They demonstrate better stability and energy conservation properties,[46] even though there are several methods considering energy conservation at the ensemble level given that imposing the energy conservation at each trajectory is too strict.[47,48,12,42] Instead of collecting information from the swarms of trajectories, the ITMQC method employs auxiliary trajectories (ATs) placed on all of the excited states for each "real" trajectory. These ATs spawned on each adiabatic state describe the spatial distribution of each adiabatic wave packet indirectly, and this information is utilized to compute the quantum momenta and vector potential needed in the XF formulation. Decoherence-induced surface hopping based on XF (DISH-XF)[49] or simply SHXF[46] is a representative of these ITMQC methods. In SHXF, the electronic propagation is modified following the XF equation, and the nuclear dynamics is simplified according to the usual SH technique. To date, the SHXF method has been used in both model and atomistic calculations.[36,50] Furthermore, the MQCXF method has been reported and can be regarded as an independent-trajectory limiting case of CTMQC. Compared to the regular Ehrenfest approach, both electronic evolution and the nuclear propagation in MQCXF are affected by the terms that originate from the XF.[51]

In this work, we present a systematic assessment and comparative analysis of several XF-based and more traditional ITMQC methods to better understand their potential and pitfalls. Whenever a new category of NA dynamics methods emerges among a myriad of existing NA dynamics methods, it is essential to clarify their benefits and limitations compared to the pool of pre-existing methods. Without detailed exploration and assessment, it is often difficult to use the newly introduced approaches with confidence, which may result in either an underappreciation of their advantages or abuse even in situations where other alternatives may perform equal or better. In particular, our focus is on the family of XF-based ITMQC methods. While the SHXF method has been exclusively tested in various models,[49,51] including the Shin−Metiu,[52] NaI,[53] Tully,[18] and Subotnik−Shenvi double-arch geometry,[28] and atomistic systems,[50,54,55] the comprehensive analysis on the whole family of XF-based ITMQC methods is still lacking, which includes a variety of model Hamiltonians and the comparison between the more traditional NA dynamics methods. Especially, the Ehrenfest variants have been restricted to simple scattering models[51] or a linear vibronic model for a uracil cation[46] with little attention to more elaborate models emphasizing multiple NA transitions over long-time scales.

To fill in the identified gap, we first implement the XF-based ITMQC methods in the Libra package,[56,57] which is already equipped with the range of traditional trajectory surface hopping (TSH) methods for NA dynamics methods as well as with fully quantum dynamics (QD) algorithms and can be used both with model Hamiltonians[58−61] and with atomistic systems.[62−67] We present a self-contained account on the theoretical grounds of the methods implemented, as well as the corresponding algorithmic details. We pay special attention to seemingly simple but practically nasty topics of state tracking and phase correction. In this Libra implementation, we ensure that they are applied consistently and timely in different parts of the algorithm and interplay correctly with the multitude of dynamical variables and parameters involved in the XF dynamics. We introduce a new branching correction (BC) method for auxiliary-trajectory (AT) dynamics for the XF methods. We also implemented the Schwartz and Subotnik time-dependent width schemes for adaptive quantum momentum calculations, as needed in the XF-based simulations.

Relying on the new implementation and the pre-existing Libra's capabilities, we conduct a comprehensive evaluation of the XF-based ITMQC methods, namely: the surface hopping with exact factorization (SHXF),[49] the mixed quantum-classical dynamics with exact factorization (MQCXF),[51] and the mean-field with exact factorization (MFXF).[46] These methods are compared to several more traditional surface hopping schemes, such as the fewest-switches surface hopping (FSSH),[18] the branching-corrected surface hopping (BCSH),[13] and the simplified decay of mixing (SDM),[21] as well as the conventional Ehrenfest (mean-field, MF) method.[19] Utilizing an extensive set of model Hamiltonians in this work, we monitor characteristic observables during the dynamics and conduct error analysis between the NA dynamics methods and the QD benchmark. We introduce quantitative metrics and scores for determining the hierarchy of NA dynamics methods, based on their capabilities to describe the evolution of state populations and coherences.

2. METHODOLOGY

2.1. Review of the XF-Based MQC Equations. First, we introduce the notation to describe various kinds of states and wave functions involved. The electron−nuclear state $|\Psi(t)\rangle$ belongs to Hilbert space $\mathcal{H}_{r\times R} = \mathcal{H}_r \otimes \mathcal{H}_R$ given by a direct product of nuclear and electronic Hilbert spaces, $\mathcal{H}_R$ and $\mathcal{H}_r$, respectively. Note also that $|\boldsymbol{R}\rangle \in \mathcal{H}_R$ and $|\boldsymbol{r}\rangle \in \mathcal{H}_r$, where $\boldsymbol{r}$ and $\boldsymbol{R}$ are electronic and nuclear coordinate states, respectively. Bolded notation is used throughout this work to refer to vectors and matrices. Whenever possible, we prefer a compact vector-matrix notation of equations to the explicit multi-index forms. By definition of the corresponding Hilbert spaces, the state vector $|\Psi(t)\rangle \in \mathcal{H}_{r\times R}$ can also be rewritten in an explicit form, $|\Psi(t)\rangle = |\chi(t), \Phi(t)\rangle$. Here, χ and Φ stand for the nuclear and electronic states. Following the XF formalism, one may then determine the marginal and conditional components

https://doi.org/10.1021/acs.jctc.4c00343
J. Chem. Theory Comput. 2024, 20, 5022−5042

of this ansatz. We choose χ as the marginal component by applying the resolution of identity to $|\Psi(t)\rangle$ with respect to $|\boldsymbol{R}\rangle \in \mathcal{H}_{\boldsymbol{R}}$, that is, $|\Psi(t)\rangle = \int d\boldsymbol{R}|\boldsymbol{R}\rangle\langle\boldsymbol{R} \mid \Psi(t)\rangle = \int d\boldsymbol{R}|\boldsymbol{R}\rangle\langle\boldsymbol{R} \mid \chi(t), \Phi(t)\rangle = \int d\boldsymbol{R} \mid \boldsymbol{R}\rangle\langle\boldsymbol{R} \mid \chi(t)\rangle \mid \Phi_{\boldsymbol{R}}(t)\rangle$. Here, the marginal nuclear state $|\chi(t)\rangle$ belongs to $\mathcal{H}_{\boldsymbol{R}}$ and the $\Phi(t)$ component of the $|\chi(t), \Phi(t)\rangle$ state becomes the conditional electronic state $|\Phi_{\boldsymbol{R}}(t)\rangle \in \mathcal{H}_{\boldsymbol{r}}$ but having the parametric dependence on $\boldsymbol{R}$ denoted by its subscript. The representation-specific wave functions are obtained by further projections $\chi(\boldsymbol{R}, t) = \langle\boldsymbol{R}|\chi(t)\rangle$, $\Phi(\boldsymbol{r}, t; \boldsymbol{R}) = \langle\boldsymbol{r}|\Phi_{\boldsymbol{R}}(t)\rangle$, where the semicolon implies a parametric dependence of the electronic wave function on nuclear coordinates, $\boldsymbol{R}$. Thus, the general state $|\Psi(t)\rangle$ can be written as $|\Psi(t)\rangle = \int d\boldsymbol{R}|\boldsymbol{R}\rangle\chi(\boldsymbol{R}, t)|\Phi_{\boldsymbol{R}}(t)\rangle \in \mathcal{H}_{\boldsymbol{r}\times\boldsymbol{R}}$ and its $\boldsymbol{R}$-projection $|\Psi(\boldsymbol{R}, t)\rangle$ gives the position-resolved molecular state defined as $|\Psi(\boldsymbol{R}', t)\rangle = \langle\boldsymbol{R}'|\Psi(t)\rangle = \int d\boldsymbol{R}\langle\boldsymbol{R}'|\boldsymbol{R}\rangle\chi(\boldsymbol{R}, t)|\Phi_{\boldsymbol{R}}(t)\rangle \int d\boldsymbol{R}\delta(\boldsymbol{R}' - \boldsymbol{R})\chi(\boldsymbol{R}, t)|\Phi_{\boldsymbol{R}}(t)\rangle = \chi(\boldsymbol{R}', t)|\Phi_{\boldsymbol{R}'}(t)\rangle \in \mathcal{H}_{\boldsymbol{r}}$.

Based on XF, the XF-based MQC equations have been formulated for trajectory-based NA dynamics:[39,40]

$$i\hbar\frac{d}{dt}|\Phi_{\boldsymbol{R}}(t)\rangle = [\hat{H}_{\mathrm{BO}}(\boldsymbol{R}(t)) + \hat{H}_{\mathrm{XF}}(\boldsymbol{R}, t)]|\Phi_{\boldsymbol{R}}(t)\rangle \tag{1a}$$

$$\begin{aligned}\hat{H}_{\mathrm{XF}}(\boldsymbol{R}, t) &= -\boldsymbol{\mathcal{P}}^{T}\boldsymbol{M}^{-1}[\boldsymbol{A} + i\hbar\nabla] \\ &= -i\hbar\boldsymbol{\mathcal{P}}^{T}\boldsymbol{M}^{-1}[|\nabla\Phi_{\boldsymbol{R}}\rangle\langle\Phi_{\boldsymbol{R}}| + |\Phi_{\boldsymbol{R}}\rangle\langle\nabla\Phi_{\boldsymbol{R}}|]\end{aligned} \tag{1b}$$

$$\dot{\boldsymbol{P}} = \boldsymbol{F} \tag{2}$$

$$\boldsymbol{F}(\boldsymbol{R}, t) = \boldsymbol{F}^{\mathrm{MF}}(\boldsymbol{R}, t) + \boldsymbol{F}^{\mathrm{XF}}(\boldsymbol{R}, t) \tag{3a}$$

$$\boldsymbol{F}^{\mathrm{MF}}(\boldsymbol{R}, t) = -\langle\Phi_{\boldsymbol{R}}(t)|\nabla\hat{H}_{\mathrm{BO}}|\Phi_{\boldsymbol{R}}(t)\rangle \tag{3b}$$

$$F_{\nu}^{\mathrm{XF}}(\boldsymbol{R}, t) = \sum_{\mu}\frac{2i\mathcal{P}_{\mu}}{\hbar M_{\mu}} \times (A_{\mu}A_{\nu} - \hbar^{2}\mathrm{Re}[\langle\nabla_{\mu}\Phi_{\boldsymbol{R}}(t) \mid \nabla_{\nu}\Phi_{\boldsymbol{R}}(t)\rangle]) \tag{3c}$$

Here, vector matrices of dynamical variables and their derivatives are column vectors containing the corresponding variables of each nuclear degree of freedom (DOF): $\boldsymbol{R} = (R_0, R_1, \cdots, R_{N_{\mathrm{dof}}-1})^T$, $\boldsymbol{P} = (P_0, P_1, \cdots, P_{N_{\mathrm{dof}}-1})^T$, $\nabla = (\partial_{R_0}, \partial_{R_1}, \cdots, \partial_{R_{N_{\mathrm{dof}}-1}})^T$, and so on. We will use this convention in the rest of the paper. $\hat{H}_{\mathrm{BO}}(\boldsymbol{R})$ is the usual Born−Oppenheimer Hamiltonian of the system, and $\hat{H}_{\mathrm{XF}}(\boldsymbol{R})$ is the electron−nuclear correlation Hamiltonian based on XF. $\boldsymbol{M}$ is the diagonal matrix containing each mass of the DOF ν as its elements, that is, $\boldsymbol{M} = \mathrm{diag}\ (M_0, M_1, \ldots M_{N_{\mathrm{dof}}-1})$, $\hbar$ is the reduced Planck's constant ($\hbar = 1$ in atomic units), and Re[*] refers to taking the real part of the corresponding expression. Note that eq 1a is already an approximation that disregards an additional term that is similar to the diagonal Born−Oppenheimer correction present in the exact treatment.

The total nuclear force, eq 3a, includes the conventional Ehrenfest or mean-field (MF) term, $\boldsymbol{F}^{\mathrm{MF}}(\boldsymbol{R}, t)$, eq 3b, as well as the decoherence force, $\boldsymbol{F}^{\mathrm{XF}}(\boldsymbol{R}, t)$, eq 3c, constructed using the time-dependent vector potential, $\boldsymbol{A}$, and quantum momentum, $\boldsymbol{\mathcal{P}}$, defined as

$$\boldsymbol{A}(\boldsymbol{R}, t) = \langle\Phi_{\boldsymbol{R}}(t)| - i\hbar\nabla\Phi_{\boldsymbol{R}}(t)\rangle \tag{4}$$

$$\mathcal{P}(\boldsymbol{R}, t) = -i\hbar\frac{\nabla|\chi(\boldsymbol{R}, t)|}{|\chi(\boldsymbol{R}, t)|} \tag{5}$$

Since both vector potential and quantum momentum depend on nuclear coordinates, computing these properties requires a differentiable representation of nuclear wave functions, $\chi(\boldsymbol{R}, t)$.

Based on the partial normalization condition, $\langle\Phi_{\boldsymbol{R}} \mid \Phi_{\boldsymbol{R}}\rangle = 1$, $\forall\ \boldsymbol{R}$, any electronic propagations with the XF decoherence (or electron−nuclear correlation) Hamiltonian, the middle part of eq 1b, can be equivalently done in terms of a spatial derivative on the electronic density operator, the rightmost expression of eq 1b.[68] Using this form of the $\hat{H}_{\mathrm{XF}}$ and the expansion of electronic basis states in adiabatic basis, $|\Phi_{\boldsymbol{R}}\rangle = |\boldsymbol{\psi}\rangle\boldsymbol{C}(\boldsymbol{R})$, it can be written in a more practical form:

$$\begin{aligned}\hat{H}_{\mathrm{XF}} &= -i\hbar\boldsymbol{\mathcal{P}}\boldsymbol{M}^{-1}(|\nabla\psi\rangle\boldsymbol{C}\boldsymbol{C}^{+}\langle\psi| + |\psi\rangle \\ &\quad ((\nabla\boldsymbol{C})\boldsymbol{C}^{+} + \boldsymbol{C}(\nabla\boldsymbol{C})^{+})\langle\psi| + |\psi\rangle\boldsymbol{C}\boldsymbol{C}^{+}\langle\nabla\psi|) \\ &\approx \sum_{\nu}\frac{-i\hbar\mathcal{P}_{\nu}}{M_{\nu}} \times |\psi\rangle(\nabla_{\nu}\rho)\langle\psi|\end{aligned} \tag{6}$$

Here, the contraction is conducted over the nuclear degrees of freedom, leaving the resulting object as an operator. Here, $|\boldsymbol{\psi}\rangle = (|\psi_0\rangle, |\psi_1\rangle, \ldots, |\psi_{N-1}\rangle)$, is the row-vector of the adiabatic basis states, $\boldsymbol{C} = (c_0, c_1, \ldots, c_{N-1})^T$ is the column-vector of the corresponding amplitudes, and $\boldsymbol{\rho} = \boldsymbol{C}\boldsymbol{C}^{+}$ is a nuclear coordinate-dependent reduced electronic density matrix. More details on this notation can be found elsewhere.[23] Here, the coupling between the quantum momentum and nonadiabatic coupling (NAC) is neglected. Thus, the XF Hamiltonian matrix in the adiabatic basis is given as

$$\boldsymbol{H}_{\mathrm{XF}} = -\sum_{\nu}\frac{i\hbar\mathcal{P}_{\nu}}{M_{\nu}} \times \nabla_{\nu}\rho \tag{7}$$

Representing the adiabatic electronic amplitudes in a polar form, $C_j(\boldsymbol{R}) = |C_j(\boldsymbol{R})|\ \exp\ (i\theta_j(\boldsymbol{R})/\hbar)$, and assuming that the phase is most sensitive to geometrical changes, their gradients can be written as

$$\nabla_{\nu}C_j \approx \frac{i}{\hbar}\nabla_{\nu}\theta_j C_j = \frac{i}{\hbar}\phi_{j\nu}C_j \tag{8}$$

In the matrix representation, the spatial derivative of the coefficient vector becomes $\nabla_{\nu}\boldsymbol{C} = \frac{i}{\hbar}\boldsymbol{\varphi}_{\nu}\boldsymbol{C}$, where $\boldsymbol{\phi}_{\nu} = \mathrm{diag}\ (\nabla_{\nu}\theta_0, \nabla_{\nu}\theta_1, \ldots\nabla_{\nu}\theta_{N-1})$, a diagonal matrix of gradients of phase factors. The key approximations in eqs 6 and 8 follow the prescriptions of Min et al.[39,40]

Finally, the $\boldsymbol{H}_{\mathrm{XF}}$ matrix is given by

$$\begin{aligned}\boldsymbol{H}_{\mathrm{XF}} &= -\sum_{\nu}\frac{i\hbar\mathcal{P}_{\nu}}{M_{\nu}} \times (\nabla_{\nu}\boldsymbol{C}\boldsymbol{C}^{\dagger} + \boldsymbol{C}\nabla_{\nu}\boldsymbol{C}^{\dagger}) \\ &= \sum_{\nu}\frac{\mathcal{P}_{\nu}}{M_{\nu}} \times (\boldsymbol{\phi}_{\nu}\boldsymbol{C}\boldsymbol{C}^{\dagger} - \boldsymbol{C}\boldsymbol{C}^{\dagger}\boldsymbol{\phi}_{\nu}) \\ &= -\sum_{\nu}\frac{\mathcal{P}_{\nu}}{M_{\nu}} \times (\boldsymbol{\rho}\boldsymbol{\phi}_{\nu} - \boldsymbol{\phi}_{\nu}\boldsymbol{\rho})\end{aligned} \tag{9a}$$

or

$$(H_{\mathrm{XF}})_{ab} = \sum_{\nu}\rho_{ab}(\phi_{\nu,aa} - \phi_{\nu,bb})\frac{\mathcal{P}_{\nu}}{M_{\nu}} \tag{9b}$$

The decoherence force is then given by

https://doi.org/10.1021/acs.jctc.4c00343
J. Chem. Theory Comput. 2024, 20, 5022−5042

Table 1. Nomenclature of the Nonadiabatic Dynamics Methods Used in This Work

method	electronic evolution	nuclear force	surface hopping/ velocity rescaling	auxiliary trajectories spawning	total energy conservation
MF, aka Ehrenfest	only $\hat{H}_{\mathrm{BO}}(\boldsymbol{R}(t))$ in eq 1a	only $\boldsymbol{F}^{\mathrm{MF}}(\boldsymbol{R}, t)$ in eq 3a	no hopping/no rescaling	no	yes
TSH (FSSH, SDM, BCSH)	only $\hat{H}_{\mathrm{BO}}(\boldsymbol{R}(t))$ in eq 1a; SDM introduced non-Hamiltonian terms	adiabatic forces of the active state in eq 3a	do hopping/do rescaling	no	enforced by velocity rescaling
MFXF, aka EhXF[a]	both $\hat{H}_{\mathrm{BO}}(\boldsymbol{R}(t))$ and $\hat{H}_{\mathrm{XF}}(\boldsymbol{R}, t)$ are used in eq 1a	only $\boldsymbol{F}^{\mathrm{MF}}(\boldsymbol{R}, t)$ in eq 3a	do hopping/no rescaling	yes $\mathcal{P}_\nu$ in eq 5 depends on the active (pointer) state.	not expected
SHXF (DISH-XF)	both $\hat{H}_{\mathrm{BO}}(\boldsymbol{R}(t))$ and $\hat{H}_{\mathrm{XF}}(\boldsymbol{R}, t)$ are used in eq 1a	adiabatic forces of the active state in eq 3a	do hopping/do rescaling	yes $\mathcal{P}_\nu$ in eq 5 and the physical trajectory depends on the active (pointer) state.	enforced by velocity rescaling
MQCXF	both $\hat{H}_{\mathrm{BO}}(\boldsymbol{R}(t))$ and $\hat{H}_{\mathrm{XF}}(\boldsymbol{R}, t)$ are used in eq 1a	both $\boldsymbol{F}^{\mathrm{MF}}(\boldsymbol{R}, t)$ and $\boldsymbol{F}^{\mathrm{XF}}(\boldsymbol{R}, t)$ are used in eq 3a	do hopping/no rescaling	yes $\mathcal{P}_\nu$ in eq 5 depends on the active (pointer) state.	yes[b]

[a]In this table, "EhXF" means an approximation of the MQCXF without the XF force and "MQCXF" means the independent-trajectory formulation of CTMQC, following ref 46. [b]The total energy conservation in MQCXF is not "perfect" around classical turning points, although the overall energy drift is alleviated using the energy-based approximation[51] defined as eq 21 in Sec 2.3.

$$F_\nu^{\mathrm{XF}} = -\frac{i}{\hbar}\sum_{a,b}\rho_{aa}\rho_{bb}\sum_{\mu}(\varphi_{\nu,bb} - \varphi_{\nu,aa})(\varphi_{\mu,bb} - \varphi_{\mu,aa})\frac{\mathcal{P}_\mu}{M_\mu} \tag{10}$$

As follows from the structure of eqs 9b and 10, the XF Hamiltonian matrix and XF (decoherence) force depend on the relative differences of phase gradients of adiabatic coefficients, e.g., $\phi_{\nu,aa} - \phi_{\nu,bb}$, the observation useful for a qualitative analysis of the decoherence forces.

We briefly summarize the hierarchy of the XF methods leading to the emergence of the ITMQC methods from the original CTMQC formalism. The CTMQC method is considered the most rigorous quantum-classical limit of XF.[39,40,69,38] In it, all trajectories evolve simultaneously following the coupled equations, eqs 1a, 1b, 2, 3a, 3b, and 3c. The quantum momentum $\mathcal{P}$, eq 5, depends on the nuclear wave function represented by all trajectories, and it affects all the trajectories. Considering that $\mathcal{P}$ can be computed for each trajectory independently, by leveraging auxiliary-trajectory basis functions (TBFs) spawned on all electronic states with nonzero populations, Min and co-workers introduced an ITMQC variation of the CTMQC with the physical trajectories described in a way similar to TSH schemes.[49] This TSH-based approach is justified by the fact that the exact time-dependent potential energy surface often resembles the adiabatic potentials[70] while the time-dependent vector potential acts in a manner reminiscent of the velocity rescaling in TSH.[71] Later, the ideas of ITMQC have been extended to the mean-field-based formulations.[51,46]

In the ITMQC methods, the XF corrections emerge as the corrections to the electronic evolution, eqs 9a and 9b, nuclear forces, eq 10, or both. The nuclei can be propagated using either the MF or adiabatic force, corrected with the XF terms or not. Depending on the chosen combinations, the total energy can be conserved either naturally or be enforced by the SH velocity rescaling algorithm, or not conserved at all. The nomenclature of possible computational schemes is summarized in Table 1. Although one can generalize it to consider various combinations of the algorithms to be used (e.g., the surface hopping could be based on the GFSH algorithm instead of the default FSSH and so on), we keep our nomenclature consistent with the prior report.[46] Also, we point out how the nomenclature of MQCXF appears differently in the literature. Originally, Ha and Min[51] have developed the MQCXF method and called this method "EhXF", considering that the nuclear dynamics is governed by the continuous force given as eq 3a. Later, Arribas et al.[46] have labeled "EhXF" as MQCXF to clarify that this method is the independent-trajectory version of CTMQC and used the same term, EhXF, for referring to its simplification, in which the XF force, eq 3c, is simply omitted and only the Ehrenfest force, eq 3b, remains. In this work, we use MFXF to specify the EhXF method for clarity.

2.2. Electronic Propagation of the XF Equations. The electronic propagation is conducted using a Trotter splitting approach and the generalized local diabatization scheme as implemented in Libra:[72,73]

$$\boldsymbol{C}' = \boldsymbol{U}_{\mathrm{XF}}\left(\boldsymbol{C}(t); \frac{\Delta t}{2}\right)\boldsymbol{C}(t) \tag{11a}$$

$$\boldsymbol{C}'' = \boldsymbol{T}\boldsymbol{U}_{\mathrm{MF}}(\Delta t)\boldsymbol{C}' \tag{11b}$$

$$\boldsymbol{C}(t + \Delta t) = \boldsymbol{U}_{\mathrm{XF}}\left(\boldsymbol{C}''; \frac{\Delta t}{2}\right)\boldsymbol{C}'' \tag{11c}$$

Here, $\boldsymbol{U}_{\mathrm{MF}}$ and $\boldsymbol{U}_{\mathrm{XF}}$ are the evolution operators in the adiabatic basis corresponding to propagation according to the $\hat{H}_{\mathrm{BO}}$ and $\hat{H}_{\mathrm{XF}}$ operators, respectively, and computed as

$$\boldsymbol{U}_{\mathrm{MF}}(\Delta t) = \exp\left(-i\frac{\boldsymbol{H}_{\mathrm{BO}}(t) + \boldsymbol{T}^{+}\boldsymbol{H}_{\mathrm{BO}}(t + \Delta t)\boldsymbol{T}}{2\hbar}\Delta t\right) \tag{12a}$$

$$\boldsymbol{U}_{\mathrm{XF}}(\boldsymbol{C}(t); \Delta t) = \exp\left(-i\frac{\boldsymbol{H}_{\mathrm{XF}}(\boldsymbol{C}(t))}{\hbar}\Delta t\right) \tag{12b}$$

Note that the evolution according to $\boldsymbol{U}_{\mathrm{XF}}$ is only approximate since the XF Hamiltonian itself depends on the amplitudes, $\boldsymbol{C}$. Thus, in principle, more sophisticated integrators could be used. However, a similar simplified integrator for the XF part, constructed locally in time, has been utilized previously and led to acceptable quality of integration.[68,74,75] As an alternative, one can resort to the fourth-order Runge−Kutta (RK4) method as in the work of Pieroni et al.[37] to handle the nonlinearity of the underlying equations. In this context, we have tested the RK4 method for XF propagation and found that both schemes give nearly identical dynamics (Section S1) using the same set of model systems.

The matrix $\boldsymbol{T}$ is the orthogonalized basis reprojection matrix, computed as

https://doi.org/10.1021/acs.jctc.4c00343
J. Chem. Theory Comput. 2024, 20, 5022−5042

$$\boldsymbol{T} = \boldsymbol{X}(\boldsymbol{P}^{-1}) \tag{13a}$$

$$\boldsymbol{X}(\boldsymbol{t}) = \boldsymbol{t}(\boldsymbol{t}^{+}\boldsymbol{t})^{-1/2} \tag{13b}$$

$$P\text{: } P_{ij} = \langle \psi_i(t) | \psi_j(t + \Delta t) \rangle \tag{13c}$$

The basis reprojection matrix, $\boldsymbol{T}$, appearing in eq 11b is a critical component of the simulation since it accounts for phase and character consistency of the propagated states. It resolves the known problems of trivial crossing[76−79] and inconsistent phases[61,80,81] of adiabatic wave function at different (even infinitesimally close) geometries.

2.3. The AT Algorithm. The AT approach enables the quantum momentum, the object that couples the trajectories, to be computed within each independent trajectory. All quantities in the present section refer to quantities belonging to a single independent trajectory. In order to compute the quantum momentum, one can recognize that eq 5 can be rewritten in a more convenient form that involves nuclear probability density, $|\chi|^2$, instead of just the nuclear wave function magnitude, $|\chi|$.

$$\mathcal{P}(\boldsymbol{R}, t) = -i\hbar \frac{\nabla |\chi|^2}{2|\chi|^2} \tag{14}$$

Thus, a differentiable representation of the nuclear probability density, $|\chi|^2$, is needed. We employ a multidimensional Gaussian approximation:

$$|\chi|^2 = \sum_i |\chi_i|^2 = \sum_i N_i \prod_\nu \exp\left(-\frac{(R_\nu - R_{i,\nu})^2}{2\sigma_{i,\nu}^2} \right) \tag{15}$$

Here, the summation is carried out over all electronic states ($i = 0, ..., N-1$), N_i is the normalization factor satisfying $|\chi_i|^2/|\chi|^2 = \rho_{ii}$ for the Gaussian on each state, $\boldsymbol{R}_i = (R_{i,0}, R_{i,1}, ..., R_{i,N_{\mathrm{dof}}-1})^T$ is the position of center of the Gaussian wave packet on the ith electronic state, and $\sigma_{i,\nu}$ is the width of ith state Gaussian along the nuclear DOF ν. Taking the width parameter to be the same for all electronic states, $\sigma_{i,\nu} = \sigma_\nu, \forall\, i$, the quantum momentum can be expressed in a more computationally convenient way:[49]

$$\mathcal{P}(\boldsymbol{R}, t) = \frac{i\hbar}{2}\sigma^{-2}(\boldsymbol{R} - \langle \boldsymbol{R} \rangle) \approx \frac{i\hbar}{2}\sigma^{-2} \sum_i \rho_{ii}(\boldsymbol{R}_a - \boldsymbol{R}_i) \tag{16}$$

Here, $\boldsymbol{\sigma}$ is the diagonal matrix containing width parameters as its elements, $\langle \boldsymbol{R} \rangle = \frac{\sum_i \boldsymbol{R}_i |\chi_i|^2}{\sum_i |\chi_i|^2}$ is the average position of the overall nuclear probability density, and $\boldsymbol{R}_a$ is the auxiliary position on an active-state AT. The ATs are propagated along the dynamics. In our implementation, the Gaussian width parameters, σ_ν, can be kept frozen or treated as time-dependent. Usually, such parameters are initialized to represent the initial nuclear probability density.

An AT for the ith electronic state is generated when the mixing criterion, $\epsilon < |C_i|^2 < 1 - \epsilon$, is satisfied. This mixing criterion is used for determining whether the electronic state is in a superposition or not. In the case that $|C_i|^2 = 0$, no adiabatic wave packet on the ith state would be involved, and when $|C_i|^2 = 1$, the electronic state corresponds to that ith adiabatic state, i.e., a pure state. The initial auxiliary position $\boldsymbol{R}_i$ and momentum $\boldsymbol{P}_i$ are set to the same values as the real position $\boldsymbol{R}$ and momentum $\boldsymbol{P}$, respectively. The motion of the AT is ballistic according to the current auxiliary momentum $\boldsymbol{P}_i$:

$$\boldsymbol{R}_i(t + \Delta t) = \boldsymbol{R}_i(t) + \boldsymbol{M}^{-1}\boldsymbol{P}_i(t)\Delta t \tag{17}$$

The auxiliary momentum at each time step is determined from the following energy conservation condition:

$$\frac{1}{2}\boldsymbol{P}_i^T\boldsymbol{M}^{-1}\boldsymbol{P}_i + E_i = \frac{1}{2}\boldsymbol{P}^T\boldsymbol{M}^{-1}\boldsymbol{P} + E \tag{18}$$

In the SHXF methods, E corresponds to the potential energy of the active (pointer) state, whereas in the MQCXF or MFXF method, E is the Ehrenfest energy given as $E = \sum_i \rho_i E_i$. The auxiliary momentum is computed as a projection of the real momentum, i.e., $\boldsymbol{P}_i := \alpha_i \boldsymbol{P}$. There are several peculiarities in determining the value of rescaling factor α_i in the auxiliary momentum calculation. Depending on the energetics of potential energy surfaces, the rescaling factor α_i may become imaginary. The propagation of an AT would become classically forbidden. In the traditional TSH approaches, this situation is known as frustrated hops. In the original implementation of SHXF, this situation is handled by setting the momenta of ATs to zero, $\alpha_i := 0$.[49] Instead of fixing the auxiliary position with the zero auxiliary momentum as above, Arribas et al. suggested projecting out the corresponding nonactive state and renormalizing the coefficients,[46] inspired by the branching-corrected (BC) surface hopping (BCSH) method.[13]

Another issue for computing AT momenta is related to the reversal of real trajectory momenta at classical turning points. Since auxiliary momenta are computed by a positive scaling of the real momenta, when the system encounters classical turning points, the directions of all existing auxiliary momenta reverse discontinuously. To address this artifact, Ha and Min[51] monitored the sign change of a dot product between the force and momenta, following the BCSH scheme as well. If the dot products $\boldsymbol{F}^T(t)\boldsymbol{P}(t)$ and $\boldsymbol{F}^T(t)\boldsymbol{P}(t - \Delta t)$ have different signs, the electronic state is collapsed to the current active state ($|C_a|^2 = 1$; $|C_{i\neq a}|^2 = 0$) and destroy all ATs. The information on the previous momenta $\boldsymbol{P}(t - \Delta t)$ is saved in the previous auxiliary momenta, so the sign of the dot product can be easily determined. In the present work, we consider a strategy to combine both BC algorithms when an AT becomes classically forbidden or a turning point is involved. In the case of the MQCXF or MFXF method, this process could lead to a collapse to a classically forbidden state and a drift in the total energy.

In all ITMQC methods, an active state is determined by the hopping probability $P_{i\to j}$ within a time interval $[t, t + \Delta t]$ according to the conventional FSSH scheme.[18]

$$P_{i\to j} = \max\left[0, \frac{2\mathrm{Re}\left[\rho_{ij}(t)d_{ij}(t)\right]}{\rho_{ii}(t)}\Delta t\right] \tag{19}$$

Here, d_{ij} is the NAC matrix element. The active state affects the calculation of quantum momenta, as in eq 16. In SHXF, the active state affects the calculation of quantum momentum and the nuclear force. However, in MQCXF or MFXF, the active state only guides the direction of decoherence, so the active state serves as a "pointer" state.[82] Even though this feature is not detailed in the original work of MQCXF,[51] the pointer state in MQCXF is crucial to capture the wave packet reflection properly. Each independent mean-field trajectory cannot "see" the overall nuclear distribution when the wave

https://doi.org/10.1021/acs.jctc.4c00343
J. Chem. Theory Comput. 2024, 20, 5022−5042

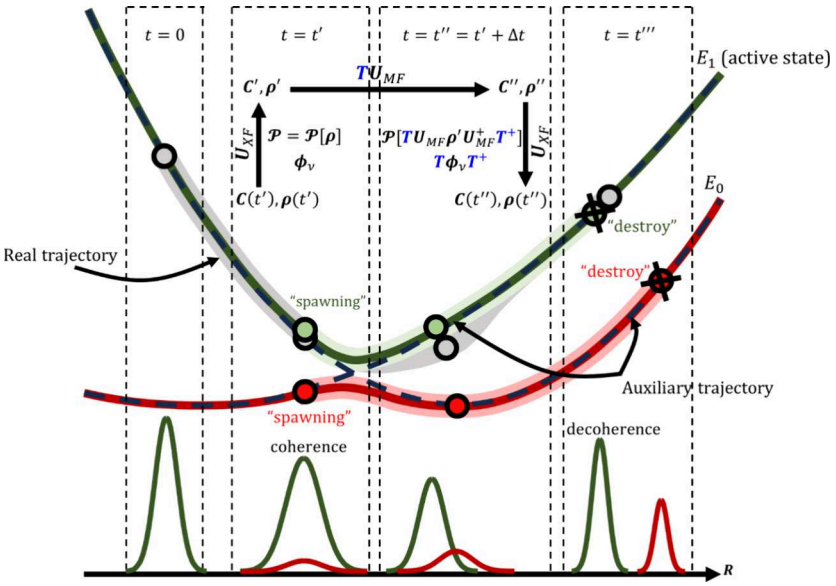

Figure 1. Schematic illustration of the auxiliary-trajectory (AT) propagation and local diabatization in MQCXF. Snapshots of each time step are distinguished by dashed boxes. Gray circles are representative classical positions on the real trajectory, while green and red circles are ones on ATs of each adiabatic state. Real and auxiliary trajectories are represented as shaded lines, and adiabatic wave packets, which should be reproduced by the statistical average of classical positions, are drawn below in the corresponding color code. If the schematic were for SHXF, the real trajectory coincided with an active-state AT when the dynamics was in coherence. The dynamics is initialized at the first excited state at $t = 0$. At $t = t'$, the dynamics encounters the crossing region and each AT is spawned. Following the local diabatization scheme, electronic propagation from $t = t'$ to $t = t''$ is conducted. Using the basis reprojection matrix $\boldsymbol{T}$, the coefficients and corresponding density matrix are reordered to $\mathbf{C}''$ and $\boldsymbol{\rho}''$, respectively. This procedure affects the quantum momenta in the second XF propagation, since the quantum momenta depend on the density matrix as in eq 16. Furthermore, the phase gradients $\boldsymbol{\phi}_\nu$ are reordered accordingly and are dependent on the coefficients as well. At $t = t'''$, the dynamics reaches decoherence to the active (pointer) state, and each AT is destroyed.

packet splits, and the resulting quantum momentum without the pointer state cannot yield proper XF force (see Section S2 for details). A hop during the dynamics initializes the ATs. When an electronic state that has satisfied the mixing criterion recovers to an adiabatic state, satisfying $|C_i|^2 > 1 - \epsilon$, the adiabatic recovery is considered to be achieved. Then, electronic coefficients are initialized to the ith state and all ATs are destroyed, mimicking the wave function collapse.

Following the original implementation of SHXF,[49] the phase gradient $\boldsymbol{\phi}_\nu$ is computed by the change of auxiliary momenta:

$$\begin{aligned}\phi_{\nu,ii}(t_i) &= 0;\ \phi_{\nu,ii}(t + \Delta t) \\ &= \phi_{\nu,ii}(t) + P_{i,\nu}(t + \Delta t) - P_{i,\nu}(t),\ t \\ &> t_i \end{aligned} \tag{20}$$

Here, t_i is the latest time when ith AT is generated. However, this computational scheme causes the violation of the energy conservation in MQCXF. To address this problem, the energy-based approximation can be used.[51]

$$\boldsymbol{\phi}_\nu = -P_\nu \frac{\boldsymbol{E}}{2(T + \delta T)} \tag{21}$$

Here, $\boldsymbol{E}$ is a diagonal matrix having each adiabatic energy as its elements, T is the kinetic energy, and δT is a masking parameter used to prevent numerical instability of eq 21 when the dynamics encounters a classical turning point ($T = 0$). In this work, we set $\delta T = 10^{-4}$ Ha. In MQCXF and MFXF, eq 21 is employed. An analogous energy-based approximation has been utilized in the works of Maitra and co-workers[42,43] and alleviated the energy conservation problem, although this method is not a perfect remedy due to the sensitivity near classical turning points. The MQCXF method conserves the total energy, except for the case of the turning-point problem and collapsing events to a classically forbidden state, while the force of MFXF is fundamentally nonenergy conserving, since the decoherence force in eq 10 is not considered in the first place. In this work, the MFXF approach does not correspond directly to the reported XF-based methods but is regarded as a variation of MQCXF for the purpose of exploring the effect of the mission of the XF force in the original MQCXF formulation. For more practical use of MFXF, one may need to investigate the energy-based approximation for MFXF, but this is outside the scope of the current work.

2.4. Time-Dependent Gaussian Width Approximations. The wave-patch width parameter σ_ν in the expression of quantum momenta, eq 16, is the key parameter in the ITMQC methods. Originally, a fixed Gaussian function was used for approximating the nuclear density $|\chi|^2$. The width parameter is usually determined by the nuclear distribution of the initial sampling. However, it is obvious that the predefined width would deviate from the exact nuclear distribution during the dynamics. To understand the possible advantages of the nonfixed Gaussian width parameters, we explore two time-dependent Gaussian width schemes.

2.4.1. The Schwartz Scheme. Schwartz and co-workers[27,83] suggested the following time-dependent width depending on the instantaneous de Broglie wavelength $\lambda_{\mathrm{D},\nu} = h/P_\nu$.

$$\sigma_\nu^{-2}(t) = \left(\frac{(w/\mathrm{Bohr})^2}{2\lambda_{\mathrm{D},\nu}(t)}\right)^2 = \left(\frac{(w/\mathrm{Bohr})^2 P_\nu}{4\pi\hbar}\right)^2 \tag{22}$$

Here, w is the so-called interaction width parameter, estimating the spatial extent of NAC. Since the decoherence algorithm in

https://doi.org/10.1021/acs.jctc.4c00343
J. Chem. Theory Comput. 2024, 20, 5022−5042

the ITMQC algorithm turns on after the dynamics has approached the coupling region, focusing on the behavior at the crossing region could be a sensible choice.

2.4.2. The Subotnik Scheme. Based on the maximum wave packet overlap conjecture proposed by Subotnik and his coworkers,[84] Ha and Min employed a time-dependent pairwise Gaussian width $\sigma_{ij,\nu}(t)$ for two-state model problems.[51]

$$\sigma_{ij,\nu}^2(t) = \hbar \frac{|R_{i,\nu} - R_{j,\nu}|}{|P_{i,\nu} - P_{j,\nu}|} \tag{23}$$

Even though this expression is originally restricted to the two-state problem, we have considered a pairwise average as its generalization.

$$\sigma_\nu^{-2}(t) = \frac{1}{N_{\mathrm{st}} - 1} \sum_{\substack{i,j=0 \\ i<j}}^{N-1} \sigma_{ij,\nu}^{-2}(t) \tag{24}$$

This is analogous to the quantum momentum calculation from pairwise ATs of Han et al.[68] It is worth noting that eq 23 allows us to have an almost "parameter-free" decoherence algorithm by replacing the Gaussian width with internal auxiliary variables. Since auxiliary variables in eq 23 are defined only when the electronic state is in a superposition, the time-dependent width is estimated only when the decoherence correction is computed. When the ith adiabatic state meets the mixing criterion ($\epsilon < |C_i|^2 < 1 - \epsilon$) at the first time, $\sigma_{ij,\nu}^2$ for all i is set to a large number (1.0×10^{10} Bohr^2 in this work), ensuring no numerical problem for the quantum momentum calculation due to a vanishing numerator in eq 23.

2.5. The Algorithm Outline. In this section, we present an explicit flow of the ITMQC dynamics algorithms (see Section S3 for the flowchart). Also, the schematic illustration of AT propagation is shown in Figure 1.

1. Trajectories are initialized by setting nuclear positions, momenta, and initial electronic state.
2. Following the velocity Verlet algorithm, update the half time-step momentum and full time-step position:

$$\boldsymbol{P}\left(t + \frac{1}{2}\Delta t\right) = \boldsymbol{P}(t) + \frac{1}{2}\Delta t \boldsymbol{F}(t)$$

$$\boldsymbol{R}(t + \Delta t) = \boldsymbol{R}(t) + \boldsymbol{M}^{-1}\boldsymbol{P}\left(t + \frac{1}{2}\Delta t\right)\Delta t$$

3. Recompute the Hamiltonian that corresponds to the updated coordinates $\boldsymbol{H}_{\mathrm{BO}}(\boldsymbol{R}(t + \Delta t))$.
4. Using the eigenstates of the prior, $\boldsymbol{H}(\boldsymbol{R}(t))$, and the updated $\boldsymbol{H}(\boldsymbol{R}(t + \Delta t))$ Hamiltonian, compute the time-overlaps matrix, $\boldsymbol{P}(t, t + \Delta t) = \langle \boldsymbol{\psi}(t) | \boldsymbol{\psi}(t + \Delta t) \rangle$, eq 13c. Using this matrix, compute the basis set reprojection matrix, $\boldsymbol{T}$ according to eqs 13a and 13b.
5. If the time-dependent Gaussian width approximation (Section 2.4) is employed, the Gaussian width is updated according to eq 22 or 23 (all XF methods). Here, any of the choices eq 22 or 23 can be used with any of the XF methods.
6. Electronic amplitudes are propagated. This procedure is done in several steps:
   - 6.1 The XF Hamiltonian, eqs 9a and 9b, is computed using the amplitudes at the initial time-step, $\boldsymbol{C}(t)$ (all XF methods).
   - 6.2 The amplitudes are propagated half time-step using the computed XF Hamiltonian, eq 11a (all XF methods).
   - 6.3 The amplitudes are propagated full time-step due to the Hamiltonian, $\boldsymbol{H}_{\mathrm{BO}}(t)$, updated previously, according to eq 11b. Note that the transformation by the basis reprojection matrix, $\boldsymbol{T}$, is applied at the end of this step to reflect reordering (and phase adjustment) of the amplitudes that correspond to the evolution of the adiabatic basis states, $|\boldsymbol{\psi}(t)\rangle \rightarrow |\boldsymbol{\psi}(t + \Delta t)\rangle$. The subsequent evolution of such amplitudes should follow the ordering of the properties computed in the new basis of adiabatic states, $|\boldsymbol{\psi}(t + \Delta t)\rangle$.
   - 6.4 In all XF methods, the phase gradients are reordered to reflect the basis transformation $|\boldsymbol{\psi}(t)\rangle \rightarrow |\boldsymbol{\psi}(t + \Delta t)\rangle$ using the basis reprojection matrix, $\boldsymbol{T}$, that is $\boldsymbol{\phi}_\nu := \boldsymbol{T}\boldsymbol{\phi}_\nu\boldsymbol{T}^+$. Note that the order of this operation is made consistent with the order of adiabatic amplitude transformations. In SHXF, we save this reordered phase gradient for the next calculation, eq 20.
   - 6.5 In all XF methods, the XF Hamiltonian is recomputed once again to reflect the effect of updated electronic amplitudes and phase gradients.
   - 6.6 In all XF methods, the amplitudes are propagated for the second half time-step using the updated XF Hamiltonian, eq 11c.
7. Active adiabatic state is updated using the basis reprojection matrix $\boldsymbol{T}$. Note that while in the TSH methods such as FSSH and SHXF, the active state determines the PES governing the evolution of nuclei; in MFXF and MQCXF, the active state is used in determining the quantum momentum, eq 5.
8. The updated force is computed $\boldsymbol{F}(t + \Delta t)$. In TSH methods including SHXF, the force corresponding to adiabatic PES of the active state is used. In the MFXF method, the Ehrenfest force is used, eq 3b. In the MQCXF, the decoherence force, eq 3c, is also added to the MF force, eq 3b.
9. The nuclear momentum is updated for the second half time-step using the updated force:

$$\boldsymbol{P}(t + \Delta t) = \boldsymbol{P}\left(t + \frac{1}{2}\Delta t\right) + \frac{1}{2}\Delta t \boldsymbol{F}(t + \Delta t)$$

10. In all XF methods, if a population $|C_i|^2$ of the ith adiabatic state, having satisfied the mixing criterion, $\epsilon < |C_i|^2 < 1 - \epsilon$, becomes larger than $1 - \epsilon$, we collapse the electronic state on the ith adiabatic basis state.
11. In all XF methods, we check the mixing criterion for each adiabatic state, $\epsilon < |C_i|^2 < 1 - \epsilon$. If this condition is satisfied at the first time, we generate the corresponding AT. If an AT no longer meets this condition, we destroy that AT.
12. For all XF methods, auxiliary positions are propagated by following eq 17.
13. For all XF methods, auxiliary momenta are computed by a projection: $\boldsymbol{P}_i := \alpha_i \boldsymbol{P}$ according to the energy conservation relation, eq 18. If $\alpha_i^2 < 0$, we set $\alpha_i := 0$ and thus $\boldsymbol{P}_i = 0$. While we propagate auxiliary momenta,

https://doi.org/10.1021/acs.jctc.4c00343
J. Chem. Theory Comput. 2024, 20, 5022−5042

we check the branching correction condition explained in Section 2.3.

13.1 If $\alpha_i^2 < 0$ and the ith state is a nonactive state, we further project out that nonactive state.

13.2 We investigate the sign of dot products between forces and momenta, $\boldsymbol{F}^T(t + \Delta t)\boldsymbol{P}(t + \Delta t)$ and $\boldsymbol{F}^T(t + \Delta t)\boldsymbol{P}(t)$.This process is done by monitoring the sign of $\boldsymbol{F}^T(t + \Delta t)\boldsymbol{P}_i(t + \Delta t) \cdot \boldsymbol{F}^T(t + \Delta t)\boldsymbol{P}_i(t)$. If this product is negative, we collapse the electronic state to the active state. If the above branching correction algorithms are activated, all ATs are destroyed. In MFXF and MQCXF, the momentum rescaling is followed additionally for the energy conservation.

14. The phase gradient, $\boldsymbol{\phi}_\nu$, is computed according to eq 20 (SHXF) or eq 21 (MFXF, MQCXF).

15. In all TSH methods, the hopping process is conducted using the hopping probability eq 19. In these methods, the hopping changes the physical state of the trajectory. In MFXF and MQCXF, only active state is updated and there is no momentum rescaling for energy conservation. When a hop occurs successfully, we destroy ATs.

2.6. Comparison between the Quantum and MQC Dynamics. In this work, the QD is performed with the discrete variable representation method[85] to provide the reference for each model dynamics. The total wave function in QD is expressed in the nuclear position grid and electronic basis $\{|a\rangle\}$ as follows.

$$|\Psi(\boldsymbol{R}, t)\rangle = \sum_{\mathrm{a}} \chi_{\mathrm{a}}(\boldsymbol{R}, t)|a\rangle \tag{25}$$

Here, $\chi_{\mathrm{a}}(\boldsymbol{R}, t)$ is the amplitude of an adiabatic wave packet on the adiabatic electronic state a and at the grid position $\boldsymbol{R}$. By evolving the time-dependent Schrödinger equation within this ansatz, the amplitudes are collected during QD. The time step of the quantum benchmark is set to 1.0 au.

For assessing the quality of each dynamics method, the Ehrenfest position $\langle \boldsymbol{R} \rangle$, adiabatic population $\langle \rho_i \rangle$ based on coefficients, the coherence indicator $\langle |\rho_{ij}|^2 \rangle$, and the gauge-invariant part of the time-dependent potential energy surface (TDPES) $\langle \Phi_{\boldsymbol{R}}|\hat{H}_{\mathrm{BO}}|\Phi_{\boldsymbol{R}}\rangle$ are calculated in the level of the quantum and trajectory-based dynamics as follows.

$$\langle \boldsymbol{R}(t) \rangle_{\mathrm{Q}} = \int \mathrm{d}\boldsymbol{R}\, \boldsymbol{R} \sum_i |\chi_i(\boldsymbol{R}, t)|^2 \tag{26a}$$

$$\langle \boldsymbol{R}(t) \rangle_{\mathrm{MQC}} = \frac{1}{N_{\mathrm{tr}}} \sum_{k=0}^{N_{\mathrm{tr}}-1} \boldsymbol{R}^k(t) \tag{26b}$$

$$\langle \rho_i(t) \rangle_{\mathrm{Q}} = \int \mathrm{d}\boldsymbol{R} |\chi_i(\boldsymbol{R}, t)|^2 \tag{27a}$$

$$\langle \rho_i(t) \rangle_{\mathrm{MQC}} = \frac{1}{N_{\mathrm{tr}}} \sum_{k=0}^{N_{\mathrm{tr}}-1} |C_i^k(t)|^2 \tag{27b}$$

$$\langle |\rho_{ij}|^2(t) \rangle_{\mathrm{Q}} = \int \mathrm{d}\boldsymbol{R} \frac{|\chi_i(\boldsymbol{R}, t)|^2 |\chi_j(\boldsymbol{R}, t)|^2}{\sum_a |\chi_a(\boldsymbol{R}, t)|^2} \tag{28a}$$

$$\langle |\rho_{ij}|^2(t) \rangle_{\mathrm{MQC}} = \frac{1}{N_{\mathrm{tr}}} \sum_{k=0}^{N_{\mathrm{tr}}-1} |C_i^k(t)|^2 |C_j^k(t)|^2 \tag{28b}$$

Here, the expressions "b" represent the quantum-classical equivalents of the corresponding quantum indicators in "a". For the SH-based methods, the adiabatic populations can be defined in terms of the occupation numbers for active states (i) of all trajectories (k), n_i^k:

$$\langle \rho_i(t) \rangle_{\mathrm{MQC}}^{\mathrm{SH}} = \frac{1}{N_{\mathrm{tr}}} \sum_{k=0}^{N_{\mathrm{tr}}-1} n_i^k \tag{29}$$

We refer to the population based on eqs 27a and 27b and eq 29 as the SE and SH populations, respectively, following the terminology used in previous works.[86,87]

Furthermore, the gauge-invariant part of the time-dependent potential energy surface (TDPES) is computed as

$$\langle \Phi_{\boldsymbol{R}}(t)|\hat{H}_{\mathrm{BO}}|\Phi_{\boldsymbol{R}}(t)\rangle = \frac{\sum_i |\chi_i(\boldsymbol{R}, t)|^2 E_i(\boldsymbol{R})}{\sum_a |\chi_a(\boldsymbol{R}, t)|^2} \tag{30}$$

Through the MQC dynamics, this quantity can be approximated by $\sum_{i=0}^{N-1} |C_i^k(t)|^2 E_i^k$ within a given set of classical trajectories,$\{\boldsymbol{R}^k(t), \boldsymbol{P}^k(t)\}$.

To systematically quantify the performance of all methods considered, we define the error metrics based on the time-integral of the mean square error (MSE) of populations and coherences obtained in approximate methods relative to the corresponding values obtained from full QD:

$$\begin{aligned} \epsilon_{\mathrm{SH/SE,pop}} &= \frac{1}{T \times N} \int_0^T \mathrm{d}t \sum_{i=0}^{N-1} [\langle \rho_i(t) \rangle_{\mathrm{Q}} - \langle \rho_i(t) \rangle_{\mathrm{MQC}}^{\mathrm{SH/SE}}]^2 \\ &\approx \frac{1}{N_{\mathrm{steps}} \times N} \sum_{\mathrm{a}=0}^{N_{\mathrm{steps}}-1} \sum_{i=0}^{N-1} [\langle \rho_i(t_{\mathrm{a}}) \rangle_{\mathrm{Q}} - \langle \rho_i(t_{\mathrm{a}}) \rangle_{\mathrm{MQC}}^{\mathrm{SH/SE}}]^2 \end{aligned} \tag{31a}$$

$$\begin{aligned} \epsilon_{\mathrm{coh}} &= \frac{2}{T \times N(N-1)} \int_0^T \mathrm{d}t \sum_{\substack{i,j=0 \\ i<j}}^{N-1} [\langle |\rho_{ij}|^2(t) \rangle_{\mathrm{Q}} \\ &\quad - \langle |\rho_{ij}|^2(t) \rangle_{\mathrm{MQC}}]^2 \\ &\approx \frac{2}{N_{\mathrm{steps}} \times N(N-1)} \sum_{\mathrm{a}=0}^{N_{\mathrm{steps}}-1} \sum_{\substack{i,j=0 \\ i<j}}^{N-1} [\langle |\rho_{ij}|^2(t_{\mathrm{a}}) \rangle_{\mathrm{Q}} \\ &\quad - \langle |\rho_{ij}|^2(t_{\mathrm{a}}) \rangle_{\mathrm{MQC}}]^2 \end{aligned} \tag{31b}$$

These metrics include averaging over all states (for SE and SH populations) or over all distinct pairs of states (for coherences). Furthermore, we define the "scores" of each method for each Hamiltonian and simulation parameters as the negative logarithms of the corresponding error values:

$$\mathrm{p}\epsilon_{\mathrm{SH/SEpop}} = -\lg(\epsilon_{\mathrm{SH/SEpop}}) \tag{32a}$$

$$\mathrm{p}\epsilon_{\mathrm{coh}} = -\lg(\epsilon_{\mathrm{coh}}) \tag{32b}$$

The higher scores correspond to smaller accumulated errors in the corresponding observables. It should be noted that such

https://doi.org/10.1021/acs.jctc.4c00343
J. Chem. Theory Comput. 2024, 20, 5022−5042

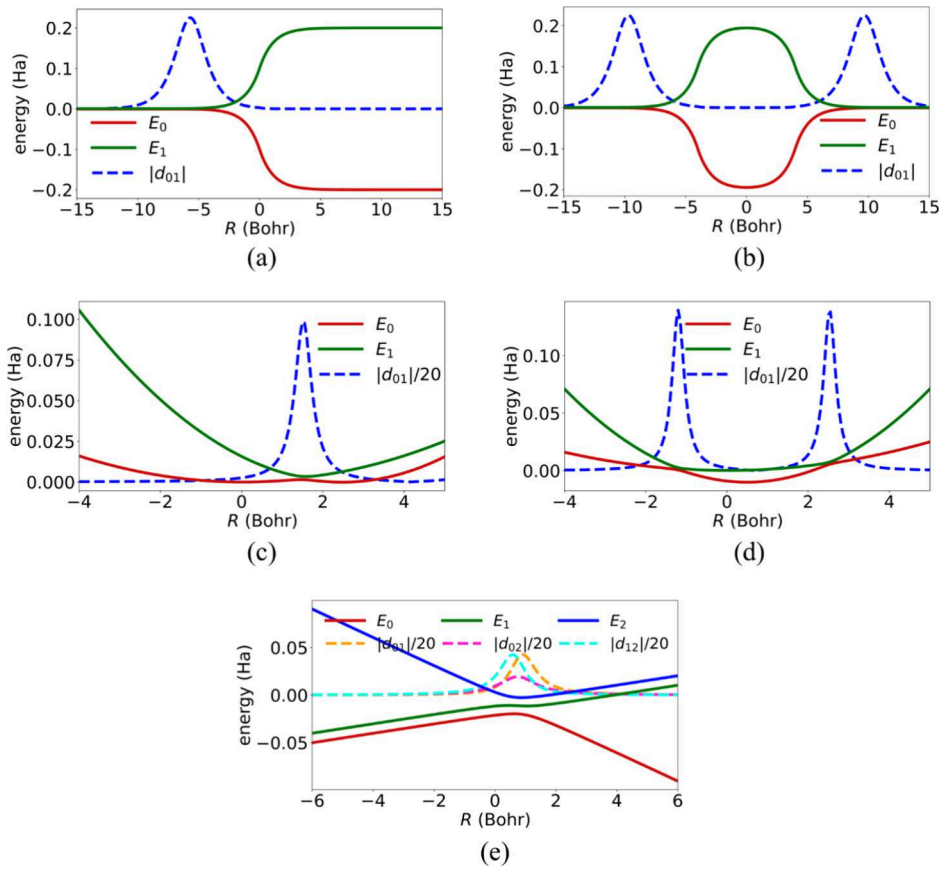

Figure 2. Adiabatic potential energy surfaces and nonadiabatic couplings of 1D model Hamiltonians in this study. (a) Tully's extended crossing with reflection (ECWR); (b) double arch geometry (DAG); (c) single-crossing (SC) Holstein model; (d) double-crossing (DC) Holstein model; (e) three-state Esch−Levine model.

scores are not necessarily indicative of the global quality of the methods, since the scores can vary depending on the parameters of the model Hamiltonian, initial conditions, or other simulation parameters. However, the scores are convenient to quantitatively compare the performance of the methods in the given context of the simulations considered in this work. To gain more global scores, one may need to average them over a broader range of simulation conditions and models, but this task goes beyond the scope of the present work.

2.7. Model Hamiltonians and Computational Details.

To assess the quality of the NA dynamics methods studied in this work, we employ five types of 1D Hamiltonians, namely, the Tully's extended crossing with reflection (ECWR),[18] Subotnik's double arch geometry (DAG),[28] single and double-crossing (SC and DC) Holstein models,[88] and three-state Esch−Levine models[89] (Figure 2). For each model Hamiltonian, electron−nuclear propagation is conducted for a time sufficient to experience multiple NA transitions: 4000 au for ECWR, 3000 au for DAG, 8000 au for Holstein models, and 8000 au for the Esch-Levine model, respectively. At the same time, the duration of propagation is chosen such that the wave packets do not evolve too far into the asymptotic regions. The mass of the nuclear degree of freedom is 2000 au.

In addition to ITMQC methods, namely, SHXF, MFXF, and MQCXF, we assess the accuracy of other conventional NA dynamics methods: mean-field (MF) or Ehrenfest dynamics, Tully's fewest-switches SH (FSSH),[18] FSSH with the simplified decay of mixing (SDM) decoherence correction,[21] and the branching-corrected surface hopping (BCSH) method.[13] Exact quantum dynamics (QD) is also conducted using the split operator Fourier transform (SOFT) method of Kosloff and Kosloff.[85] The results of the QD simulations are considered the reference and are used to assess the performance of other methods. In all trajectory-based simulations, the nuclear and electronic integration time steps are chosen to be the same and are set to 1.0 au. The initial nuclear coordinate and momentum are sampled from a Gaussian distribution that corresponds to the probability density of the ground state of a harmonic potential with a force constant of 0.01 Ha/Bohr^2. We use 2000 initial conditions to start independent trajectories. The observables of interest are averaged over these trajectories. For the ITMQC methods with a fixed Gaussian width parameter, the value of σ_ν = 0.3 Bohr in eq 15 is utilized.

The QD simulations are conducted using an integration time step of 1.0 au and a uniform grid width of 0.025 Bohr except for the Esch−Levine model dynamics, where the grid width is set to 0.020 Bohr to ensure proper propagation with large nuclear momenta. The initial wave function in such calculations is chosen as a Gaussian with the width that corresponds to the harmonic oscillator force constant of 0.01 Ha/Bohr^2. This wave packet is placed on the adiabatic state of interest. The SOFT integration is conducted in the diabatic representation, and the corresponding adiabatic properties are computed according to the underlying transformation.

Finally, we explore the use of time-dependent Gaussian width in defining quantum momenta within the ITMQC

https://doi.org/10.1021/acs.jctc.4c00343
J. Chem. Theory Comput. 2024, 20, 5022−5042

schemes. Through calculations with the time-dependent width parameters, we evaluate the role of such an approximation on the quality of the computed results. All computations are conducted using the Libra package, version 5.6.0.[89]

3. RESULTS AND DISCUSSION

3.1. Comparison of the ITMQC and Conventional Methods. In this section, we present the results of the quantum- and trajectory-based dynamics simulations using the ITMQC and conventional methods as explained in Section 2.7 and applied to various model Hamiltonians. For the ITMQC methods, we apply the fixed-width Gaussian approximation, σ = 0.3 Bohr and the BC algorithm (13.1 and 13.2 in Section 2.5). For the phase gradient calculation, we adopt the original approach (eq 20) for SHXF and the energy-based approximation (eq 21) for MFXF and MQCXF.

A. ECWR and DAG Models. The ECWR and DAG models are chosen as the simplest testbeds for this study. The parametrization of the diabatic Hamiltonians is the same with the previous study of Ha and Min.[51] The initial parameters (Table 2) are selected to allow the dynamics to pass through the coupling region, while evolving on the first excited state is classically forbidden. All SH-based methods conserve the total energy, while MFXF and MQCXF show drifts of the total energy (Figure 3a,b). The lack of total energy conservation in MFXF is inherited from its construction (Table 1): While the electronic Hamiltonian includes decoherence terms, the decoherence force is excluded from the nuclear propagation. One can observe strong total energy drifts in MFXF dynamics at the times when the decoherence correction is activated with the mixing criterion fulfilled under the NAC (Figure 3a,b). Using MQCXF, the total energy drift is relatively weak and occurs mainly due to the wave function collapse events activated at classical turning points. Thus, the total energy drift is gained when the particle is reflected at the coupling region.

Table 2. Time Durations and Initial Conditions of the Model Dynamics Simulation

	time duration, a.u.	mean position, a.u.	mean momentum, a.u.	initial adiabatic state
ECWR	4000	−15.0	25.0	0
DAG	3000	−20.0	20.0	0
SC Holstein	8000	−4.0	0.0	0
DC Holstein	8000	−4.0	0.0	0
Esch−Levine	8000	−1.0	10.0	2

Total energy conservation is critical for correctly describing the dynamics. Due to the large total energy drift observed in MFXF dynamics, the corresponding trajectories are qualitatively wrong: They are more prone to traverse through the excited-state potential energy surfaces, showing reduced chances of reflection (Section S4, Figure S10). This traversing portion of trajectories yields qualitatively different behavior of the mean coordinate as a function of time (Figure 3). Here, both MFXF and regular MF yield incorrect trajectories while both SHXF and MQCXF show perfect agreement with the reference calculations (Figure 3c,d). In fact, all the conventional TSH-based methods, even those without the decoherence correction, are able to capture this reflection behavior.

As expected, a severe "overcoherence" is observed in MF and FSSH calculations—the coherence does not decay past the moment the particle traversed the strong NAC region (Figure 3e,f). Interestingly, both MFXF and SDM show too fast decay of coherence in the ECWR model. The coherence measure decays to zero whereas the reference QD calculation suggests a convergence to the 0.1 value. In the DAG model, both MFXF and SDM show a better agreement with the reference value, although still being distinct from the QD result. At the same time, SHXF, MQCXF, and BCSH show a perfect or nearly perfect agreement with the coherence indicator from the QD simulations.

As far as the population dynamics goes, all methods but MFXF, MF, and FSSH yield a good overall agreement with the QD reference for the ECWR model. In the DAG model with a more localized region of NAC, all methods yield similar population dynamics although MFXF starts showing a crossing

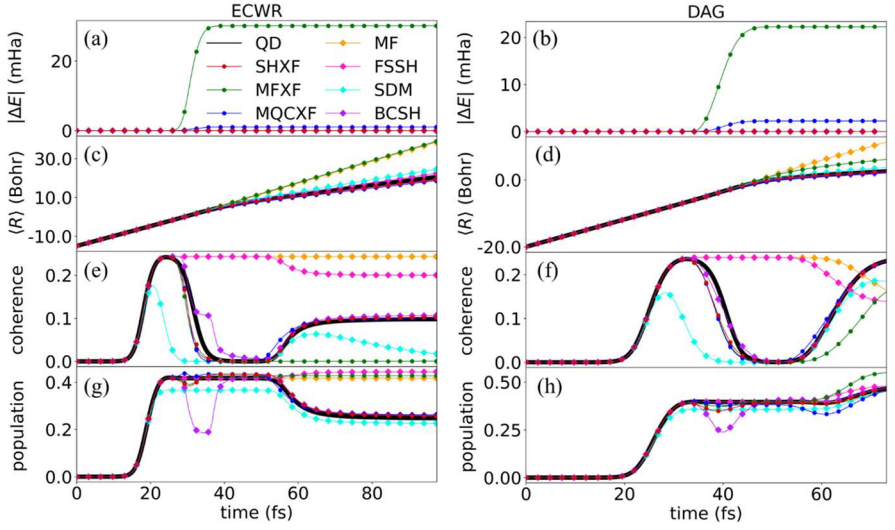

Figure 3. Characteristic observables during the nonadiabatic dynamics for the (a, c, e, g) ECWR and (b, d, f, h) DAG models. (a, b) Total energy deviation, $|E(t) - E(0)|$, (c, d) Ehrenfest positions $\langle R \rangle$, (e, f) coherences, and (g, h) excited-state populations as a function of time. In both figures, the same color code is used for distinguishing results of each dynamics method and markers are used additionally for the trajectory-based dynamics.

https://doi.org/10.1021/acs.jctc.4c00343
J. Chem. Theory Comput. 2024, 20, 5022−5042

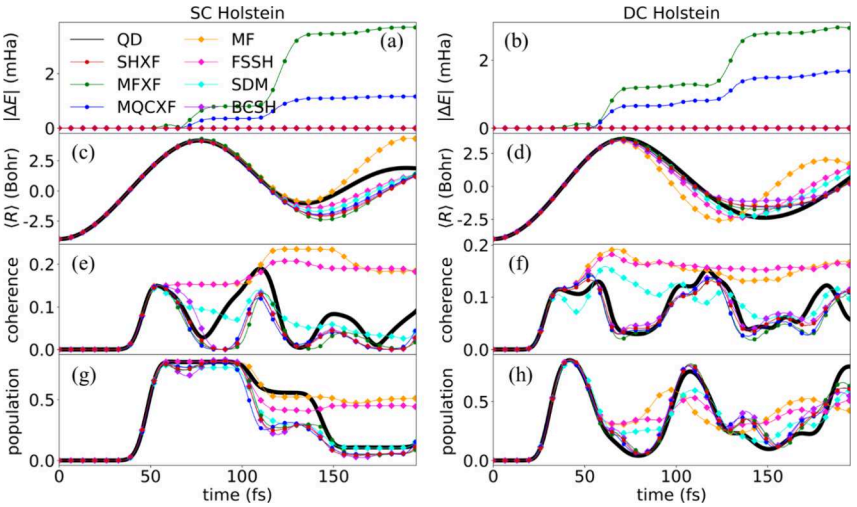

Figure 4. Characteristic observables during the nonadiabatic dynamics for the (a, c, e, g) SC and (b, d, f, h) DC Holstein models. (a, b) Total energy deviation, $|E(t) - E(0)|$, (c, d) Ehrenfest positions $\langle R \rangle$, (e, f) coherences and (g, h) excited-state populations as a function of time. In both figures, the same color code is used for distinguishing results of each dynamics method, and markers are used additionally for trajectory-based dynamics.

of the state populations in the long-time limit. The BCSH dynamics exhibits surprising "bumps" of the population curves at $t = \sim 35$ fs. This is because its population is based on the coefficients that decohere instantaneously by the branching correction algorithm in BCSH, when the dynamics encounters a classical turning point. Due to a close similarity of the population dynamics produced by different methods, the coherence indicator is an important way to distinguish and quantify the quality of trajectory-based NA dynamics methods.

B. Holstein Models. Holstein model dynamics is simulated to observe multiple NA transitions as the nuclear DOF oscillates back and forth along the bound potential energy surface. The diabatic Hamiltonian $H(R)$ for two-state Holstein models is defined as

$$H_{nn} = E_n + \frac{1}{2}k_n(R - R_n)^2,\ n = 0,\ 1 \tag{33a}$$

$$H_{01} = V \tag{33b}$$

with (a) $E_0 = E_1 = 0$, $R_0 = 0$, $R_1 = 2.5$, $k_0 = 0.002$, $k_1 = 0.005$, and $V = 0.001$ and (b) $E_0 = 0$, $E_1 = -0.01$, $R_0 = 0$, $R_1 = 0.5$, $k_0 = 0.002$, $k_1 = 0.008$, and $V = 0.001$ for the SC and DC Holstein models, respectively. All parameters are given in the atomic unit.

Similar to ECWR and DAG models, MFXF and MQCXF methods show an increase of the total energy conservation error for both Holstein models (Figure 4a,b). As before, the drift is much more dramatic for the MFXF method. The nuclear motion computed with all methods deviates from the quantum case in the long-time limit; however, the deviation seen for the MF method is the most pronounced and starts earlier than for other methods (Figure 4c,d).

As before, the coherences predicted by the MF and FSSH methods are totally incorrect for both models (Figure 4e,f), except for the simulation period when the nonadiabatic coupling region is met by the system for the first time ($t <$ 50 fs). This behavior is expected due to the overcoherent nature of the MF and FSSH schemes. These methods also fail to produce accurate populations in the longer-time limit of the simulations, especially for the SC Holstein model (Figure 4g,h). All other methods, SHXF, MFXF, MQCXF, BCSH, and SDM—are capable of reasonably reproducing coherences and populations for both models.

It is interesting to observe that for the DC Holstein model, the methods tend to predict both coherences and population better than those in the SC model. With the two coupling regions in one direction of the position space, NAC contributes more to the coherence than to spatial overlap. Thus, for such a model, the dynamics is dominated by electronic transitions and occurs in a more coherent regime. Therefore, the trajectory-based dynamics can capture the coherence better in the DC Holstein model than it does in the SC Holstein model. In the latter case, the coupling regions are less dominant and the dynamics is more strongly affected by the wave packet overlap decay, which contributes to the coherence measure. This is because the free motion of wave packets on different surfaces is more probable. Since such motion leads to decay of wave packet overlaps, the mechanism of coherence loss, it is more important and more difficult to account for decoherence effects in this regime. This is why there are greater errors in the coherence in the SC Holstein model. It is also interesting to note that the coherences from the SDM dynamics are rather close to the reference QD results, even though they deviate quite significantly from the coherence computed by other methods (Figure 4e).

To illustrate the role of wave packet overlap in determining electronic coherences, we analyze snapshots of the dynamics for the SC Holstein model (Figure 5). As seen in the snapshot for $t = 87.8$ fs (Figure 5d), the missing coherence in Figure 4e originates from the wave function overlap. The ITMQC methods cannot describe the coherence resulting from an (accidental) overlap, since the population transfer only occurs when the NAC is finite.[68] For resolving missing coherence rigorously, one may need to consider the coupling of the trajectories as in CTMQC. Even though the original CTMQC method cannot capture the coherence originating from the accidental wave packet overlap,[68] an alternative CTMQC framework that could present a new coherence descriptor and fix the coherence problem may still be possible to develop in future. Also, utilizing quantum trajectories based on Bohmian mechanics would be another candidate.[60,90,91] After the first

https://doi.org/10.1021/acs.jctc.4c00343
J. Chem. Theory Comput. 2024, 20, 5022−5042

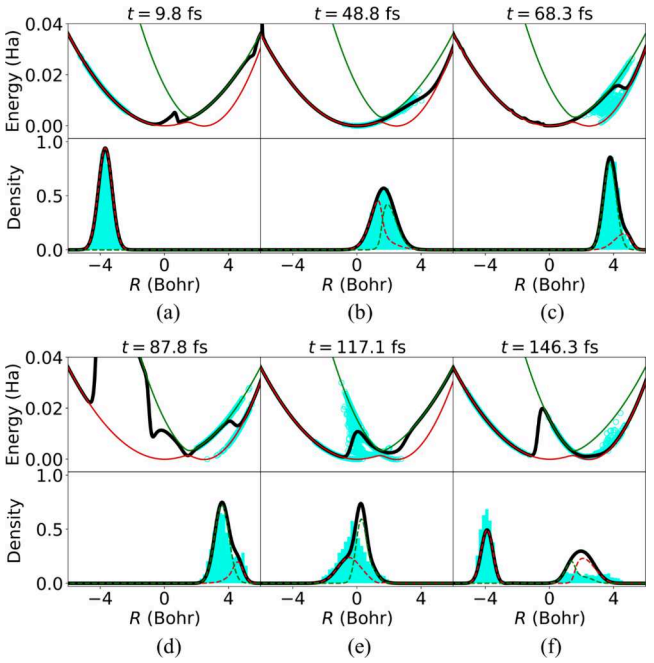

Figure 5. Snapshots of the MQCXF and quantum dynamics (QD) for the single-crossing (SC) Holstein model. The gauge-invariant part of the time-dependent potential energy surface $\langle \Phi_R | \hat{H}_{BO} | \Phi_R \rangle$ in QD (black solid line) and the potential energy of each MQCXF trajectory (cyan circles) are given, while the adiabatic potential energy surfaces are drawn for the reference, in the first panel of each snapshot. The exact nuclear density and each adiabatic wave packet density from QD and classical nuclear distribution are shown as a histogram from MQCXF in the second panel with the same color code.

NA transition, the classical trajectories are separated, propagating on each adiabatic PES. These branched trajectory-based wave packets behave independently toward the end of the dynamics. This independent behavior of the trajectories causes only a partial capture of the gauge-invariant part of TDPES at t = 68.3 fs (Figure 5c) and t = 117.1 fs (Figure 5e). Due to the discrepancy of the coherence (t = 117.1 fs), the nuclear distribution of trajectory-based wave packets at the end is different from the QD's as seen in the snapshot at t = 146.3 fs (Figure 5f).

Notably, the trajectories from the MQCXF method cascade around the coupling region (t = 68.3 and t = 117.1 fs), instead of following a single potential step as seen in the previous CTMQC studies.[45] This is because, unlike the CTMQC method, the trajectories in the MQCXF do not share the same centroid of adiabatic wave packets but all have distinct centers computed based on their own ATs. This situation also holds true for other ITMQC algorithms. In this sense, the motion predicted by the MQCXF method is similar to that originating from the SHXF method. The NA transitions can occur at any position with a finite NAC, but the switches between adiabatic states are "delayed" by following a continuous potential.

C. Three-State Esch−Levine Model. We test the methods' performance when applied to a three-state Esch−Levine model. The corresponding diabatic Hamiltonian is given by

$$H_{00} = -w_0 R,\ w_0 > 0 \tag{34a}$$

$$H_{11} = w_1 R - \delta \tag{34b}$$

$$H_{22} = w_1 R - 2\delta \tag{34c}$$

$$H_{01} = H_{02} = H_{10} = H_{20} = k \tag{34d}$$

$$H_{12} = H_{21} = 0 \tag{34e}$$

with w_0 = 0.015, w_1 = 0.005, δ = 0.01, and k = 0.005 in the atomic unit. What differentiates the three-state Esch−Levine model from the previous model systems the most is that both bound and unbound motions are possible at different regions simultaneously.

As for previous models, we observe that the MFXF has a poor energy conservation; however, the MQCXF shows a significantly smaller energy drift for the Esch−Levine Hamiltonian than for other models (Figure 6a). This is because the wave packet collapse events are much less frequent in this model, since the turning points can be met only near the region of the surfaces crossing points. Once the system passes through this region, there is little chance it may return back, at least for the current choice of the initial conditions.

Expectedly, the MF gives a poor description of the average position of the system. In fact, at a longer time, it suggests a qualitatively incorrect recoil behavior. This behavior originates from overpopulating the higher excited states (1 and 2) with the negative direction of the adiabatic forces at longer time (as indeed seen in Figure 6b). As a result, the MF force becomes negative and leads to a reversal of the average-position trajectories. For all other methods, the mean position agrees with the reference value for the whole duration of simulation, although we observe a small deviation for FSSH, MFXF, and

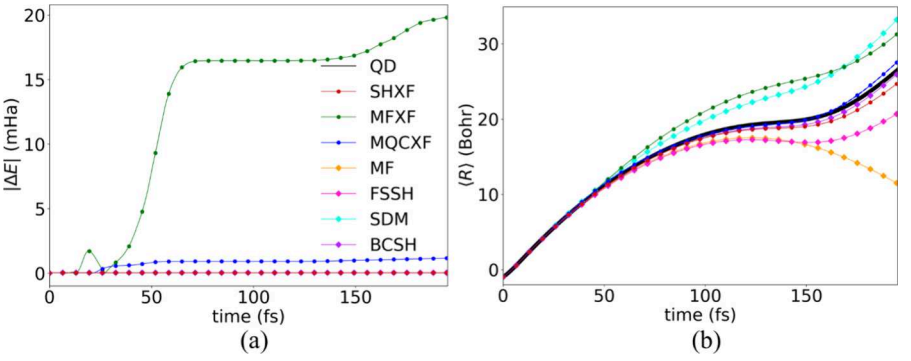

Figure 6. Evolution of total energy drift and average nuclear coordinate in nonadiabatic dynamics simulations with the three-state Esch−Levine model. (a) Total energy deviation, $|E(t) - E(0)|$ and (b) Ehrenfest positions $\langle R \rangle$ as a function of time for the three-state Esch−Levine model. Different colors are used for distinguishing results of each dynamics method, and markers are used additionally for trajectory-based dynamics.

https://doi.org/10.1021/acs.jctc.4c00343
J. Chem. Theory Comput. 2024, 20, 5022−5042

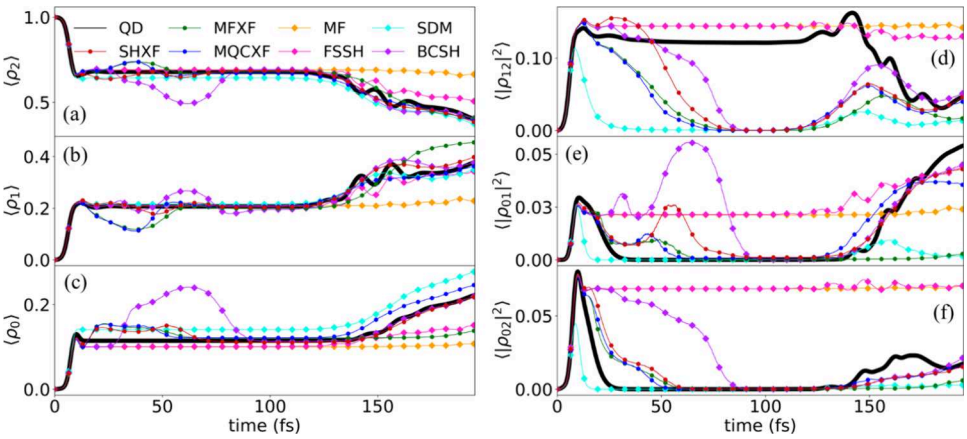

Figure 7. Reduced electronic density matrix elements from the nonadiabatic dynamics for the three-state Esch−Levine model. (Left, a−c) populations (right, d−f) coherences as a function of time for the three-state Esch−Levine model. Different colors are used for distinguishing results of each dynamics method, and markers are used additionally for the trajectory-based dynamics.

SDM methods at the end of simulation period. Yet, such deviations are qualitatively correct (correct direction).

Out of all methods, SHXF and MQCXF show the most consistent and accurate population dynamics of all states (Figure 7a−c). Importantly, these methods yield a good agreement with the QD population not only in the short-time interval but also in the longer time limit. SDM shows the second best performance, although slightly overestimating the population of the ground state. The populations produced by BCSH are also rather consistent with the QM reference, especially in the asymptotic region of longer times. However, unphysical "bumps" are observed in the shorter time interval corresponding to trajectories passing the state crossing region. In this region, the trajectory reflection events may occur as prescribed by the BCSH, leading to such "bumps" in the population. The "bumps" can be regarded a manifestation of a "delayed decoherence"—a less dramatic version of the fully overcoherent regime than the one realized in the Tully scattering models as well as in other unbound problems. In such models, trajectories may evolve into zero-NAC regions yet containing nondecayed coherences (e.g., Figure 1). In the present unbound system, the coherences also exist, even in regions with negligible NACs. However, when the density matrix collapses instantaneously due to the trajectory reflection events, the coherences decay, yielding the "bumps". We note that even though the appearance of "bump" may look unphysical and disturbing, this behavior of coherences is still more accurate than the nondecaying behavior in traditional TSH approaches, where coherences may remain notable indefinitely. It is in this sense that the "bumps" can be regarded as a less dramatic case of fully overcoherent behavior. We note that such bumps can also be observed for the ECWR and DAG models for similar reasons. In these cases, the trajectory reflection can induce wave function collapses, yielding notable variations of coherences and populations. Similar bumps are also present in the ITMQC methods (MQCXF, SHXF, and MFXF) due to the BC of ATs. However, their deviations in coherence and population are smaller in those methods because the corresponding electronic equation contains the decoherence term that improves the consistency of electronic dynamics with the wave function collapsing induced by the BC algorithm. Finally, the FSSH and MFXF show a varied quality that deteriorates at the end of the simulation interval while MF populations are dramatically different from the reference values, as noted above. The deviation of the MF populations from the QD values is also facilitated by the divergence of the corresponding nuclear trajectories, as discussed above. The divergence of populations and trajectories for the MF reinforces each other.

The differences in the coherence dynamics are very pronounced for this model and strongly depend on the chosen method (Figure 7d−f). First, almost all methods show too fast decay of ρ_{12} coherence (Figure 7d) whereas the two most unfavorable methods so far, FSSH and MF, work particularly well in this case, likely by a chance. Both FSSH and MF largely overestimate the coherences for other pairs of states and preserve them for nearly the whole duration of the simulation. The second least favorable approach here is BCSH, which produces large spurious coherences for ρ_{01} and ρ_{02}. However, it correctly captures the coherence behavior in longer time limit. The SDM method shows a good initial decay of the ρ_{01} and ρ_{02} coherences but has difficulties in capturing the coherence revivals at a later time. Finally, the ITMQC methods lead to the best (although not ideal yet) coherence dynamics on average. As noted previously, they have difficulties in modeling persistent ρ_{12} coherence at shorter times. They also may exhibit unphysical coherence "bumps", but at a much smaller scale than in BCSH. However, most of them (except for MFXF) are capable of capturing the revival of ρ_{01} and ρ_{02} coherences at longer times.

We present a more detailed analysis of the MQCXF and QD dynamics in Figure 8. The trajectories pass the surface crossing region already at t = 9.8 fs, keeping most of the population on the highest state 2 but already start populating states 1 and 0. The presence of nonzero amplitudes on each of these states leads to a raise of coherences for all three pairs as seen in Figure 7d−f. At t = 19.5 fs, some portion of trajectories cascades down to the ground state, following the gauge-invariant part of TDPES in that computed from the QD (Figure 8b, black line). At t = 39.0 fs (Figure 8c), the trajectories on the ground state diverge significantly from the trajectories on states 1 and 2, resulting in a decay of wave packet overlaps and hence in a decay of coherences ρ_{01} and ρ_{02}, consistent with results in Figure 7e,f. After the first passage of the NAC region, the coherent evolution of wave packets on states 2 and 1 persists until about t = 150 fs due to the corresponding PES being parallel and the corresponding trajectories occupying an overlapping region of space (Figure

https://doi.org/10.1021/acs.jctc.4c00343
J. Chem. Theory Comput. 2024, 20, 5022−5042

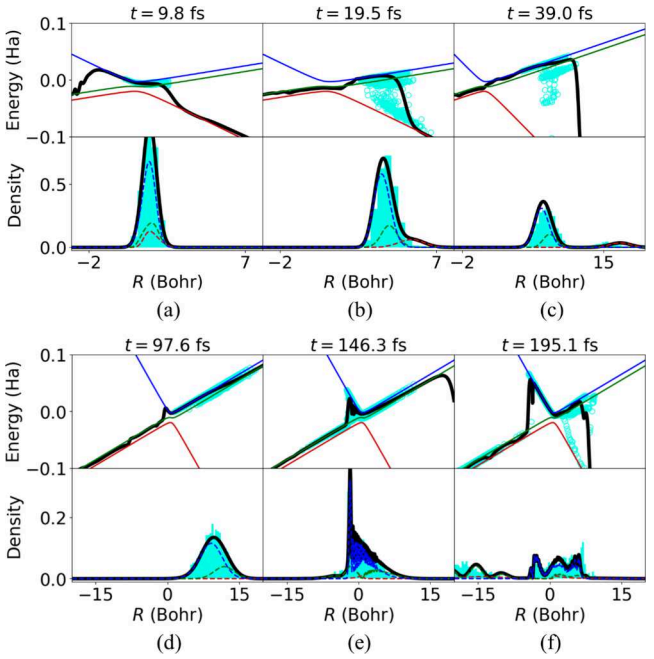

Figure 8. Snapshots of the MQCXF and quantum dynamics (QD) for the 3-state Esch-Levine model. The code of the figure is analogous to that in Figure 5.

8d,e). This spatial overlap yields a constant coherence between the first and second excited states $\langle|\rho_{12}|^2\rangle$ in QD, while this is missing in trajectory-based dynamics as seen in Figure 7d. Starting at this time (t = 146.3 fs, Figure 8e and t = 195.1 fs, Figure 8f), trajectories pass the surface crossing region for the second time and bifurcate between states 2 and 1 (leading to decay of ρ_{21} coherence) and later branch to state 0. The latter process causes the revival of ρ_{01} and ρ_{02} coherences at a later time.

D. Accuracy Assessment. Finally, we compare the quality of the methods using the accuracy metrics defined in eqs 31a, 31b, 32a, and 32b and computed for each model Hamiltonian separately (Figure 9). Generally, the SH population scores (Figure 9a) are somewhat higher than the SE population scores (Figure 9b), suggesting that having trajectory representation improves the accuracy of the results compared to the corresponding mean values derived directly from the TD-SE solution. On average, these scores vary in intervals of 2.5−3.2 and 2.2−3.0 for SH and SE populations, respectively. Among all methods, the SHXF has the highest average $p\epsilon_{\mathrm{SH,pop}}$ score slightly above 3.0. This method also shows the highest average $p\epsilon_{\mathrm{SE,pop}}$ score, slightly below 3.0. The MQCXF average $p\epsilon_{\mathrm{SE,pop}}$ score is the second largest. Note that there is no $p\epsilon_{\mathrm{SH,pop}}$ score for this method as well as for MF and MFXF since the active state in these MF-based XF algorithms only guides the decoherence indirectly. The average coherence scores differ to a larger extent across the methods (Figure 9c). Both MF and FSSH show rather low average coherence scores of about 2.0, followed by SDM and MFXF with average scores around 2.5−2.7. The SHXF and MQCXF methods show even higher average coherence scores of 3.0. Surprisingly, the BCSH method yields an even higher average coherence score.

The comparison of the average scores should be taken with the grain of salt, since the scores are strongly affected by the identities of model Hamiltonians; thus, the average scores do not represent the global accuracy of the methods, only their accuracy when applied to particular models. We observe that the population scores are typically higher for the unbound models, such as ECWR and DAG, compared to the semibound cases such as Esch−Levine and especially the bound cases SC and DC Holstein models. This effect can be rationalized as described in the above discussion. In the bound systems, the regions of nonadiabatic coupling are passed more frequently, leading to more frequent population exchange. Thus, error accumulation is faster in the bound systems, leading to lower population scores. As far as the coherence scores are concerned, there is no clear correlation between the accuracy scores and the type of model.

To summarize, the performance ranking of the methods for predicting the population is SHXF > MQCXF > BCSH > SDM ≈ MFXF > FSSH ≈ MF, and for coherence, it is BCSH > SHXF > MQCXF > MFXF > SDM > FSSH ≈ MF. However, as previously seen, MFXF is not desirable to use, since it suffers from incorrect nuclear motions due to the nonenergy conserving force.

In addition to the error measurement for the population and coherence, we present the accuracy metric for the average position $\langle R\rangle$ by the use of the normalized mean square error (Section S5, Figure S18).[92] In terms of predicting $\langle R\rangle$, SHXF, MQCXF, and BCSH have achieved high scores.

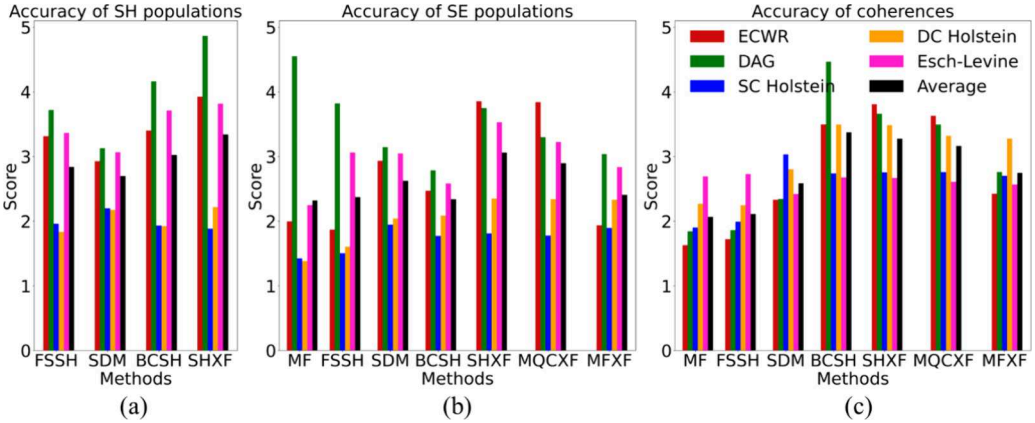

Figure 9. Accuracy scores for various models and method: (a) $p\epsilon_{\mathrm{SH,pop}}$, only for methods that define SH populations; (b) $p\epsilon_{\mathrm{SE,pop}}$; (c) $p\epsilon_{\mathrm{SE,coh}}$. The color codes of all of the panels are identical.

https://doi.org/10.1021/acs.jctc.4c00343
J. Chem. Theory Comput. 2024, 20, 5022−5042

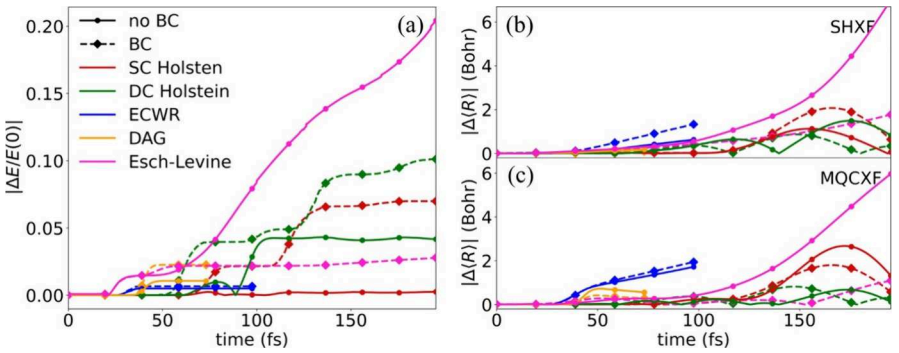

Figure 10. Differences in the model simulations using the SHXF and MQC dynamics with or without the branching correction (BC) algorithm. (a) Normalized total energy deviations in MQCXF and (b, c) Ehrenfest position deviations from the quantum dynamics in SHXF and MQCXF. Results without the BC algorithm are depicted by solid lines with circles, whereas those with the correction use dashed lines with diamonds. Results are presented for the duration of each model dynamics. A consistent color code is applied across (a−c).

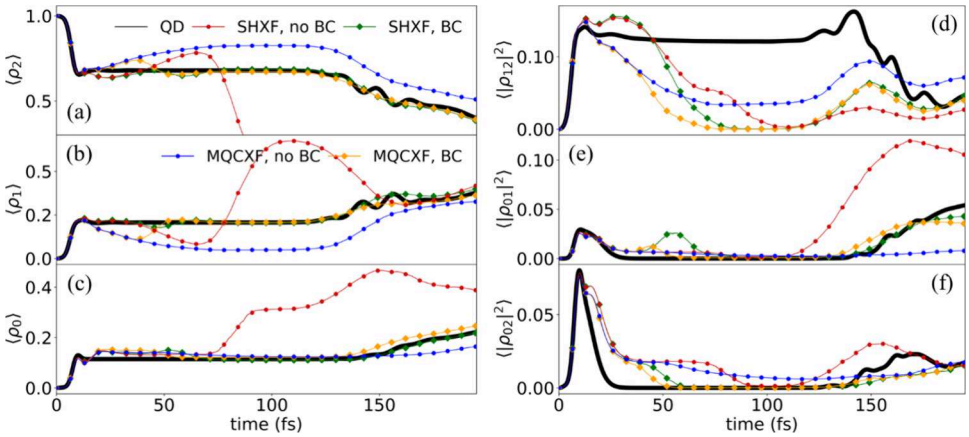

Figure 11. Reduced electronic density matrix elements from the SHXF and MQCXF dynamics with or without the branching correction (BC) algorithm for the three-state Esch−Levine model. (a−c) populations and (d−f) coherences as a function of time for the three-state Esch−Levine model, with or without the branching correction algorithm.

3.2. Impact of the BC Algorithm. In this section, we discuss the impact of the BC algorithm on ITMQC dynamics. The BC algorithm is introduced to prevent the unphysical behavior of ATs when real trajectories meet the turning points, as explained in Section 2.3. However, utilizing the BC algorithm can worsen the energy conservation in MQCXF, since the collapse to forbidden states can be facilitated by such a correction. In order to assess its influence of BC on the XF-based methods' (SHXF and MQCXF only) accuracy, we conduct the simulations using the models listed in Table 2 under the same conditions as in Section 3.1 except for turning off the BC algorithm (13.1 and 13.2 in Section 2.5). First, we monitor the deviation of the total energy and Ehrenfest position from the corresponding exact values. Even though the Ehrenfest position only quantifies the average nuclear position and should not be directly interpreted as positions of any realistic trajectories, the $\langle R \rangle$ value is still useful for discussing qualitative difference in the nuclear dynamics computed with different approaches. Furthermore, the change of the curvature the $\langle R \rangle$ function of time gives useful hints on the prevailing behavior of trajectories: whether they exhibit any branching or reflections or simply transmit the NA coupling regions. Except for the Esch−Levine model, the BC algorithm has a negative impact on energy conservation, leading to larger total energy drift when BC is utilized (Figure 10a). The Ehrenfest positions are relatively weakly affected by using the BC or not (Figure 10b,c). The BC correction proves to be important for the Esch−Levine model both in SHXF and MQCXF, since one observes an increasingly growing deviation of the average position from the corresponding QM reference.

The magnitude of the energy drift is particularly large in the Esch−Levine model when no BC is applied. These deviations arise from the energetics of the Esch−Levine model. Without the BC algorithm, the direction of the auxiliary momenta is reversed discontinuously at classical turning points. In the Esch−Levine model, the magnitude of auxiliary momenta is particularly large, since the dynamics is considerably accelerated along the slanted PES with the initial mean momentum 10.0 a.u (Figure 2e and Table 2). This makes the effect of the sign change in auxiliary momenta more critical in the Esch−Levine case than in the other model systems. The reversed auxiliary momenta directly influence the phase gradient calculation in eq 20, and the auxiliary positions propagated by these auxiliary momenta lead to incorrect quantum momenta, as given in eq 16. The discontinuous reverse in the auxiliary momenta without BC and resulting quantum momenta over trajectories are shown in Section S6, Figures S19 and 20, panels a, c, e, and g.

Consistent with large energy drift and mean position deviations in the Esch−Levine model, we also observe a notable difference in the population and coherence dynamics for this model depending on whether the BC is applied or not

https://doi.org/10.1021/acs.jctc.4c00343
J. Chem. Theory Comput. 2024, 20, 5022−5042

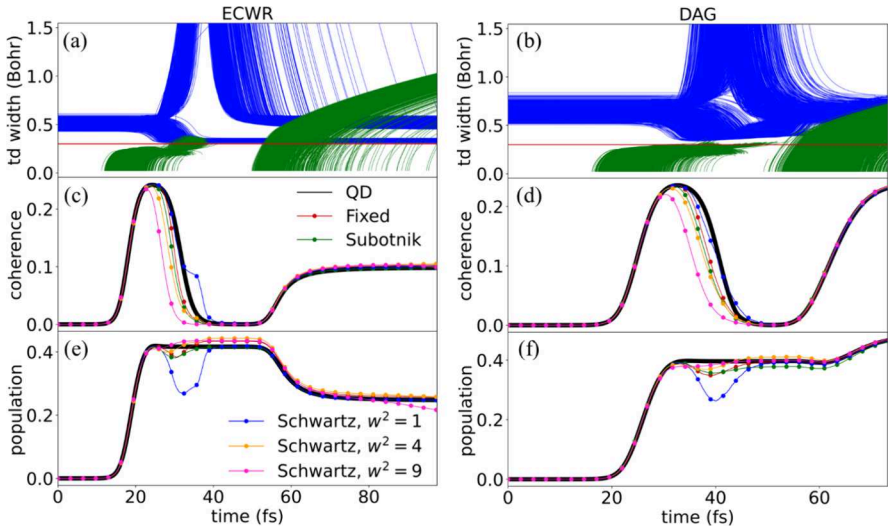

Figure 12. Characteristic observables during the SHXF dynamics with the time-dependent width approximations for (a, c, e) ECWR and (b, d, f) DAG models. (a, b) Time-dependent Gaussian widths of all trajectories, (c, d) coherences, and (e, f) populations in the SHXF dynamics as a function of time. In (a) and (b), the time-dependent width of the higher-w^2 Schwartz approximations (w^2 = 4, 9 Bohr^2) are omitted for conciseness since they behave similarly to the case of w^2 = 1 Bohr^2 except for their reduced magnitudes in line with eq 22. The widths from the Subotnik scheme are shown only when the decoherence algorithm is activated.

(Figure 11). As the analysis of the population plots suggests, both SHXF and MQCXF yield populations nearly matching the corresponding quantum reference while not including this correction leads to notable nonphysical deviations of the computed populations. The difference in the state population computed with SHXF or MQCXF can be attributed to the following factor. In MQCXF, the phase gradient calculation is unaffected by the sign change of auxiliary momenta, since it relies on the energy-based approximation, eq 21. Nonetheless, the BC algorithm still impacts the calculation of quantum momenta (eq 16) in MQCXF since the position displacement $R - \langle R \rangle$ in eq 16 is affected by the auxiliary momenta.

Thus, we suggest that BC is an important component of the algorithm even though it may lead to drifts of the total energy. The latter is, however, expected since the motion of the ATs is ballistic and consequently not consistent with the total Hamiltonian of the system.

The effect of the BC algorithm is also quantified using the accuracy metric as defined in eqs 31a, 31b, 32a, and 32b (Section S7, Figure S21). As highlighted in the previous analysis, the Esch−Levine dynamics presents the most pronounced difference depending on whether the BC algorithm is activated or not. The differences in the unbound systems (ECWR and DAG) follow the next, with the least effect in the bound Holstein models. The effect of the BC algorithm largely depends on the amount of possible kinetic energy or the magnitude of nuclear momenta during the dynamics. Furthermore, the BC algorithm improves the prediction of coherence, even though its influence is less prominent than that in the population prediction (Section S7, Figure S21c). Thus, employing the BC algorithm is highly preferred in the ITMQC methods.

3.3. Time-Dependent Gaussian Width Analysis. In addition to the above analyses, we explore the effects of the time-dependent Gaussian width approximation in the SHXF and MQCXF methods using the model systems listed in Table 2. We utilize the BC algorithm (13.1 and 13.2 in Section 2.5). For the phase gradient calculation, we adopt the original approach (eq 20) for SHXF and the energy-based approximation (eq 21) for MFXF and MQCXF. The Schwartz and Subotnik approximations (eqs 22−24) are used for calculating the time-dependent Gaussian width. In the Schwartz scheme, we consider three interaction width parameters, namely, w^2 = 1,4,9 Bohr^2 for investigating their influence on the dynamics. For the Subotnik scheme, setting a parameter for the Gaussian width is unnecessary, as the width is determined by the internal auxiliary variables during the dynamics.

We present the ECWR and DAG dynamics as the representative results since the feature of time-dependent width is particularly prominent for these unbound models. By monitoring the behavior of the time-dependent widths, we observe that the widths from the Schwartz and Subotnik schemes behave in significantly different manners. The Schwartz width, based on the instantaneous de Broglie length (eq 22), diverges when the dynamics undergoes the reflection. Notably, there are two branches of the Schwartz widths, indicating the reflecting and transmitting events. On the contrary, the Subotnik widths gradually increase in accordance with the displacement of auxiliary variables along the AT propagation (eq 23). The average Subotnik widths for ECWR and DAG are 0.42 ± 0.27 and 0.30 ± 0.14 Bohr, respectively. These numbers are close to the predefined fixed width, 0.3 Bohr used in the analyses above, and the dynamics with the fixed-width and Subotnik approximation are similar indeed. This observation suggests that one may estimate reasonable widths using the Subotnik scheme and use their averages as a starting point for further optimization of the dynamics.

Overall, the coherences and populations are well reproduced, even though spurious bumps are found when the low-w^2 Schwartz width values are employed (Figure 12). This effect can be seen in the time intervals of [30, 40] fs for ECWR (Figure 12c,e) and [35, 45] fs for DAG (Figure 12f), where population and/or coherence curves have notable deviations from the exact results. At these moments, Schwartz widths (Figure 12a,b) gain large values, especially for the case of w^2 = 1. This means that the magnitude of the decoherence correction is relatively small since the quantum momenta are inversely proportional to the square of the width (eq 16). In

https://doi.org/10.1021/acs.jctc.4c00343
J. Chem. Theory Comput. 2024, 20, 5022−5042

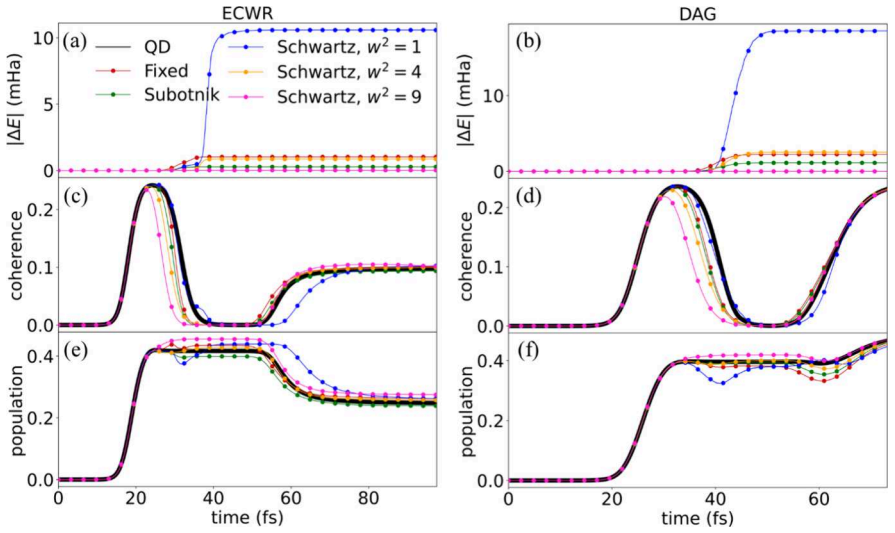

Figure 13. Characteristic observables during the MQCXF dynamics with the time-dependent width approximations for (a, c, e) ECWR and (b, d, f) DAG models. (a, b) Total energy deviation, $|E(t) - E(0)|$, (c, d) coherences, and (e, f) populations in the MQCXF dynamics for the ECWR and DAG models.

this scenario, the dynamics become very close to that of BCSH, where the population of each trajectory behaves coherently, eventually leading to an abrupt collapse due to the BC algorithm. Using the higher values of w^2 mitigates these bumps, although the coherences are underestimated to a larger extent. As seen from Figure 12, values of the Swartz parameter $w^2 = 4$ Bohr^2 are optimal for both the ECWR and DAG models since they deliver a good balance between the description of coherences and populations. The Subotnik's approach to define the time-dependent widths yields values significantly smaller than those of the Schwartz approach with small w^2 parameters (Figure 12a,b). As a result, the coherence correction is notable and no unphysical population drops are observed. The Subotnik's width increases in time, which is also a physically meaningful behavior. Indeed, in these unbound models, the wave packets should completely decohere in the long-time limit, which corresponds to small decoherence correction or large width parameter.

We also computed the MQCXF dynamics with the above time-dependent width schemes (Figure 13). The overall trends in the dynamics are similar to those found in SHXF simulations except for the lowest-w^2 Schwartz width. The MQCXF dynamics with the lowest w^2 suffers from a larger total energy deviation than the others (Figure 13a). This is also due to the weak decoherence correction, arising from a large width. Abrupt collapses to a classically forbidden state in the middle of mixing, triggered by the BC algorithm, cause large jump in the total energy, explaining the lack of energy conservation in this method. Thus, using too large widths (and weak decoherence correction) in MQCXF simulation should be avoided as it is detrimental to its quality. Stated differently, using larger Swartz w^2 parameters improves the accuracy of the population and coherence dynamics, helps avoid unphysical population drops (or coherence shoulders), and improves the quality of the total energy conservation in the MQCXF dynamics.

Finally, we evaluate the accuracy of each time-dependent width approximation using the previous accuracy metric, eqs 31a, 31b, 32a, and 32b, for the population and coherences (Section S8, Figure S23). The overall accuracy scores are similar regardless of the time-dependent width approximations. One can possibly observe more dramatic results when the initial nuclear distribution is broader.[51] It is noteworthy that both the Subotnik and Schwartz schemes can yield similar results in the Esch−Levine model. Away from the coupling region, the wave packet should be spread out, and its momenta become large following its unbound PES. However, according to the formula of the Schwartz scheme, eq 22, the width decreases as the momenta increase. Thus, the key consideration is clearly whether an "interaction width" near the crossing region can be captured, rather than describing the width over the entire time domain. Tuning the dynamics by adjusting the w^2 parameters can be done in the Schwartz scheme, while the error due to undercoherence can be accumulated when the value of w^2 is increased as seen in Section S8, Figure S23c,d.

4. CONCLUSIONS

In this work, we have presented a detailed assessment of the MFXF, MQCXF, and SHXF methods based on XF theory following their implementation in the open-source Libra package. A particular care is taken about the BC algorithm for ATs, state, and phase tracking in electronic integration of the corresponding XF-based equations using the local diabatization scheme, and about the corresponding transformations in computing quantum momentum. Using the present implementation, we conduct a comprehensive comparative study of the XF-based approaches and several conventional TSH methods: FSSH, SDM, BCSH, and MF using carefully designed 1D model Hamiltonians that yield the dynamics in distinct regimes. We introduce the accuracy scores based on the time integrals of the MSE for populations and coherences and use them to quantitatively compare and rank the considered methods.

Out of the tested methods, the MFXF shows the worst quality of energy conservation and therefore is not recommended, even though it may lead to reasonable population and coherence dynamics in short-time simulations. The rest of the tested methods can be ranked as follows: SHXF ≈ MQCXF > BCSH > SDM > FSSH ≫ MF. The MQCXF

https://doi.org/10.1021/acs.jctc.4c00343
J. Chem. Theory Comput. 2024, 20, 5022−5042

method exhibits a moderate to large drifts in total energy due to wave function collapses that cannot obey the total energy conservation condition (where TSH methods would have a frustrated hop) but is generally consistent with the QD results both in terms of populations and coherences, especially in the long-time limit, where the traditional TSH methods may already accumulate larger errors. The performance of the SHXF often exceeds that of MQCXF and QD. Considering it has no problems with energy conservation, SHXF is the recommended approach.

Surprisingly, simple decoherence methods such as BCSH and SDM often yield rather good agreement with QD populations or coherences. For some models, BCSH shows a higher score than even that of the SHXF method. We identify several intrinsic deficiencies in these methods. First, BCSH may show spurious "bumps" in population dynamics as well as lead to locally overcoherent dynamics in some situations. However, it tends to yield reasonable asymptotic behavior of coherences and populations in longer simulations. These spurious bumps can be excluded using the SH population, even though it still has an internal consistency problem between the SE and SH populations. The SDM approach is limited in its capacity to consistently produce nonvanishing coherences in longer simulation times, including the coherence revivals.

We also make several observations regarding the validity of various methods in several regimes of the anticipated dynamics, as defined by model Hamiltonians. First, the dynamics in models with multiple NAC regions (e.g., DAG or DC Holstein) is dominated by the electronic transitions, where coherence effects prevail. For these models or dynamic regimes, even simple methods without decoherence corrections such as FSSH perform rather well. In this regime, coherences are easier to describe correctly but methods may show larger errors in describing populations. Second, the dynamics in models with few NAC regions (ECWR, SC Holstein, Esch−Levine models) are more strongly affected by the wave packet divergences. In this regime, the population dynamics is easier to describe but coherences are not. In this regime, it is much more important to account for decoherence effects. One of the implications of such findings is that the methodology assessment efforts need to employ both kinds of models and explore accuracy criteria that are based on both populations and coherences. As an example, the Esch−Levine model manifests itself as a good test problem for methods incorporating decoherence corrections. The branching dynamics determines the nontrivial behavior of electronic coherences, including coherence revivals due to wave packet interference effects. The models of this kind should be fruitful testbeds for methods introducing decoherence corrections. However, one should keep in mind that coherence dynamics is not defined solely by the topology of PESs but also by the population transfer effects. Thus, having parallel surfaces does not guarantee persistent coherences, and vice versa, the coherences may persist between states with differently sloped PESs.

We find that the branching correction is very important for producing accurate population and coherence dynamics with XF methods, although it introduces the total energy drift in the MQCXF method. Without the BC algorithm, auxiliary momenta change abruptly at turning points. This change leads to unphysical AT propagation, consequently leading to incorrect calculations of the phase gradients and quantum momenta. This issue becomes particularly pronounced in systems with a high kinetic energy, as observed in the Esch−Levine dynamics. Employing the BC algorithm significantly enhances the accuracy of predicting the population and coherence. Thus, its use in ITMQC dynamics is highly recommended.

Finally, we highlight the effects of time-dependent width approximations. We find that employing a fixed-width approach with the meticulously selected width parameter is sufficient to gain good accuracy in population and coherence dynamics. Selecting Gaussian width parameters that are too large can cause unreliable results in XF methods combined with the BC algorithms, especially in MQCXF. Using the parameter-free width scheme of Subotnik yields accurate results comparable to those with the optimized width parameter. We find that Subotnik's and Schwartz schemes for time-dependent width parameters behave in qualitatively different manners, with the former yielding more reliable results. Thus, the adaptive scheme of Subotnik is recommended when no a priori estimates of the width parameters are available.

■ ASSOCIATED CONTENT

Supporting Information

The Supporting Information is available free of charge at https://pubs.acs.org/doi/10.1021/acs.jctc.4c00343.

Test of the fourth-order Runge-Kutta method for electronic propagation, the discussion of importance of the use of a pointer state in MQCXF, the flowchart for all trajectory-based methods in this work, trajectory-resolved positions and momenta, the error measures based on average position, auxiliary momenta reversal without the branching correction, Population and coherence scores depending on whether the branching correction algorithm and time-dependent Gaussian width approximations are applied, respectively (PDF)

■ AUTHOR INFORMATION

Corresponding Author

Alexey V. Akimov − *Department of Chemistry, University at Buffalo, The State University of New York, Buffalo, New York 14260, United States;* orcid.org/0000-0002-7815-3731; Email: alexeyak@buffalo.edu

Author

Daeho Han − *Department of Chemistry, University at Buffalo, The State University of New York, Buffalo, New York 14260, United States;* orcid.org/0000-0003-2853-6571

Complete contact information is available at: https://pubs.acs.org/10.1021/acs.jctc.4c00343

Notes

The authors declare no competing financial interest.

■ ACKNOWLEDGMENTS

A.V.A acknowledges the financial support of the National Science Foundation (Grant OAC-NSF-1931366). Computational support is provided by the Center for Computational Research at the University at Buffalo.

■ REFERENCES

(1) Li, Q.; Orcutt, K.; Cook, R. L.; Sabines-Chesterking, J.; Tong, A. L.; Schlau-Cohen, G. S.; Zhang, X.; Fleming, G. R.; Whaley, K. B.

Single-Photon Absorption and Emission from a Natural Photosynthetic Complex. *Nature* **2023**, *619* (7969), 300−304.
(2) Scholes, G. D.; Fleming, G. R.; Chen, L. X.; Aspuru-Guzik, A.; Buchleitner, A.; Coker, D. F.; Engel, G. S.; van Grondelle, R.; Ishizaki, A.; Jonas, D. M.; Lundeen, J. S.; McCusker, J. K.; Mukamel, S.; Ogilvie, J. P.; Olaya-Castro, A.; Ratner, M. A.; Spano, F. C.; Whaley, K. B.; Zhu, X. Using Coherence to Enhance Function in Chemical and Biophysical Systems. *Nature* **2017**, *543* (7647), 647−656.
(3) Romero, E.; Novoderezhkin, V. I.; van Grondelle, R. Quantum Design of Photosynthesis for Bio-Inspired Solar-Energy Conversion. *Nature* **2017**, *543* (7645), 355−365.
(4) Müller, K.; Schellhammer, K. S.; Gräßler, N.; Debnath, B.; Liu, F.; Krupskaya, Y.; Leo, K.; Knupfer, M.; Ortmann, F. Directed Exciton Transport Highways in Organic Semiconductors. *Nat. Commun.* **2023**, *14* (1), 5599.
(5) Sneyd, A. J.; Fukui, T.; Paleček, D.; Prodhan, S.; Wagner, I.; Zhang, Y.; Sung, J.; Collins, S. M.; Slater, T. J. A.; Andaji-Garmaroudi, Z.; MacFarlane, L. R.; Garcia-Hernandez, J. D.; Wang, L.; Whittell, G. R.; Hodgkiss, J. M.; Chen, K.; Beljonne, D.; Manners, I.; Friend, R. H.; Rao, A. Efficient Energy Transport in an Organic Semiconductor Mediated by Transient Exciton Delocalization. *Sci. Adv.* **2021**, *7* (32), No. eabh4232.
(6) Fang, Y.; Hou, Y.; Fu, X.; Wang, X. Semiconducting Polymers for Oxygen Evolution Reaction under Light Illumination. *Chem. Rev.* **2022**, *122* (3), 4204−4256.
(7) Zhao, D.; Wang, Y.; Dong, C.-L.; Huang, Y.-C.; Chen, J.; Xue, F.; Shen, S.; Guo, L. Boron-Doped Nitrogen-Deficient Carbon Nitride-Based Z-Scheme Heterostructures for Photocatalytic Overall Water Splitting. *Nat. Energy* **2021**, *6* (4), 388−397.
(8) Craig, C. F.; Duncan, W. R.; Prezhdo, O. V. Trajectory Surface Hopping in the Time-Dependent Kohn-Sham Approach for Electron-Nuclear Dynamics. *Phys. Rev. Lett.* **2005**, *95* (16), No. 163001.
(9) Zhu, C.; Nangia, S.; Jasper, A. W.; Truhlar, D. G. Coherent Switching with Decay of Mixing: An Improved Treatment of Electronic Coherence for Non-Born−Oppenheimer Trajectories. *J. Chem. Phys.* **2004**, *121* (16), 7658−7670.
(10) Jaeger, H. M.; Fischer, S.; Prezhdo, O. V. Decoherence-Induced Surface Hopping. *J. Chem. Phys.* **2012**, *137* (22), 22A545.
(11) Wang, L.; Trivedi, D.; Prezhdo, O. V. Global Flux Surface Hopping Approach for Mixed Quantum-Classical Dynamics. *J. Chem. Theory Comput.* **2014**, *10* (9), 3598−3605.
(12) Martens, C. C. Surface Hopping without Momentum Jumps: A Quantum-Trajectory-Based Approach to nonadiabatic Dynamics. *J. Phys. Chem. A* **2019**, *123* (5), 1110−1128.
(13) Xu, J.; Wang, L. Branching Corrected Surface Hopping: Resetting Wavefunction Coefficients Based on Judgement of Wave Packet Reflection. *J. Chem. Phys.* **2019**, *150* (16), 164101.
(14) Runeson, J. E.; Manolopoulos, D. E. A Multi-State Mapping Approach to Surface Hopping. *J. Chem. Phys.* **2023**, *159* (9), No. 094115.
(15) Crespo-Otero, R.; Barbatti, M. Recent Advances and Perspectives on nonadiabatic Mixed Quantum−Classical Dynamics. *Chem. Rev.* **2018**, *118* (15), 7026−7068.
(16) Jain, A.; Sindhu, A. Pedagogical Overview of the Fewest Switches Surface Hopping Method. *ACS Omega* **2022**, *7* (50), 45810−45824.
(17) Wang, L.; Akimov, A.; Prezhdo, O. V. Recent Progress in Surface Hopping: 2011−2015. *J. Phys. Chem. Lett.* **2016**, *7* (11), 2100−2112.
(18) Tully, J. C. Molecular Dynamics with Electronic Transitions. *J. Chem. Phys.* **1990**, *93* (2), 1061−1071.
(19) Ehrenfest, P. Bemerkung über die angenäherte Gültigkeit der klassischen Mechanik innerhalb der Quantenmechanik. *Z. Für Phys.* **1927**, *45* (7), 455−457.
(20) Shu, Y.; Zhang, L.; Mai, S.; Sun, S.; González, L.; Truhlar, D. G. Implementation of Coherent Switching with Decay of Mixing into the SHARC Program. *J. Chem. Theory Comput.* **2020**, *16* (6), 3464−3475.
(21) Granucci, G.; Persico, M. Critical Appraisal of the Fewest Switches Algorithm for Surface Hopping. *J. Chem. Phys.* **2007**, *126* (13), 134114.
(22) Smith, B.; Akimov, A. V. A Comparative Analysis of Surface Hopping Acceptance and Decoherence Algorithms within the Neglect of Back-Reaction Approximation. *J. Chem. Phys.* **2019**, *151* (12), 124107.
(23) Akimov, A. V. Fundamentals of Trajectory-Based Methods for nonadiabatic Dynamics. In *Comprehensive Computational Chemistry* (First ed.); Yáñez, M.; Boyd, R. J., Eds.; Elsevier: Oxford, 2024; pp 235−272. DOI: 10.1016/B978-0-12-821978-2.00034-9.
(24) Hack, M. D.; Truhlar, D. G. A Natural Decay of Mixing Algorithm for Non-Born−Oppenheimer Trajectories. *J. Chem. Phys.* **2001**, *114* (21), 9305−9314.
(25) Cheng, S. C.; Zhu, C.; Liang, K. K.; Lin, S. H.; Truhlar, D. G. Algorithmic Decoherence Time for Decay-of-Mixing Non−Born−Oppenheimer Dynamics. *J. Chem. Phys.* **2008**, *129* (2), No. 024112.
(26) Jasper, A. W.; Truhlar, D. G. Electronic Decoherence Time for Non-Born-Oppenheimer Trajectories. *J. Chem. Phys.* **2005**, *123* (6), No. 064103.
(27) Bedard-Hearn, M. J.; Larsen, R. E.; Schwartz, B. J. Mean-Field Dynamics with Stochastic Decoherence (MF-SD): A New Algorithm for nonadiabatic Mixed Quantum/Classical Molecular-Dynamics Simulations with Nuclear-Induced Decoherence. *J. Chem. Phys.* **2005**, *123* (23), 234106.
(28) Subotnik, J. E.; Shenvi, N. A New Approach to Decoherence and Momentum Rescaling in the Surface Hopping Algorithm. *J. Chem. Phys.* **2011**, *134* (2), No. 024105.
(29) Jain, A.; Alguire, E.; Subotnik, J. E. An Efficient, Augmented Surface Hopping Algorithm That Includes Decoherence for Use in Large-Scale Simulations. *J. Chem. Theory Comput.* **2016**, *12* (11), 5256−5268.
(30) Mukamel, S. *Principles of Nonlinear Optical Spectroscopy*; Oxford series in optical and imaging sciences; Oxford University Press: New York, 1995.
(31) Zhang, Z.; Long, R.; Tokina, M. V.; Prezhdo, O. V. Interplay between Localized and Free Charge Carriers Can Explain Hot Fluorescence in the CH3NH3PbBr3 Perovskite: Time-Domain Ab Initio Analysis. *J. Am. Chem. Soc.* **2017**, *139* (48), 17327−17333.
(32) Zhang, Z.; Fang, W.-H.; Tokina, M. V.; Long, R.; Prezhdo, O. V. Rapid Decoherence Suppresses Charge Recombination in Multi-Layer 2D Halide Perovskites: Time-Domain Ab Initio Analysis. *Nano Lett.* **2018**, *18* (4), 2459−2466.
(33) Ben-Nun, M.; Martínez, T. J. A Multiple Spawning Approach to Tunneling Dynamics. *J. Chem. Phys.* **2000**, *112* (14), 6113−6121.
(34) Mignolet, B.; Curchod, B. F. E. A Walk through the Approximations of Ab Initio Multiple Spawning. *J. Chem. Phys.* **2018**, *148* (13), 134110.
(35) Min, S. K.; Agostini, F.; Tavernelli, I.; Gross, E. K. U. Ab Initio nonadiabatic Dynamics with Coupled Trajectories: A Rigorous Approach to Quantum (De)Coherence. *J. Phys. Chem. Lett.* **2017**, *8* (13), 3048−3055.
(36) Vindel-Zandbergen, P.; Matsika, S.; Maitra, N. T. Exact-Factorization-Based Surface Hopping for Multistate Dynamics. *J. Phys. Chem. Lett.* **2022**, *13* (7), 1785−1790.
(37) Pieroni, C.; Sangiogo Gil, E.; Ibele, L. M.; Persico, M.; Granucci, G.; Agostini, F. Investigating the Photodynamics of Trans-Azobenzene with Coupled Trajectories. *J. Chem. Theory Comput.* **2024**, *20* (2), 580−596.
(38) Abedi, A.; Maitra, N. T.; Gross, E. K. U. Exact Factorization of the Time-Dependent Electron-Nuclear Wave Function. *Phys. Rev. Lett.* **2010**, *105* (12), 123002.
(39) Agostini, F.; Min, S. K.; Abedi, A.; Gross, E. K. U. Quantum-Classical nonadiabatic Dynamics: Coupled- vs Independent-Trajectory Methods. *J. Chem. Theory Comput.* **2016**, *12* (5), 2127−2143.
(40) Min, S. K.; Agostini, F.; Gross, E. K. U. Coupled-Trajectory Quantum-Classical Approach to Electronic Decoherence in nonadiabatic Processes. *Phys. Rev. Lett.* **2015**, *115* (7), No. 073001.

(41) Agostini, F.; Tavernelli, I.; Ciccotti, G. Nuclear Quantum Effects in Electronic (Non)Adiabatic Dynamics. *Eur. Phys. J. B* **2018**, *91* (7), 139.
(42) Arribas, E. V.; Ibele, L. M.; Lauvergnat, D.; Maitra, N. T.; Agostini, F. Significance of Energy Conservation in Coupled-Trajectory Approaches to nonadiabatic Dynamics. *J. Chem. Theory Comput.* **2023**, *19* (21), 7787−7800.
(43) Arribas, E. V.; Maitra, N. T. Energy-Conserving Coupled Trajectory Mixed Quantum−Classical Dynamics. *J. Chem. Phys.* **2023**, *158* (16), 161105.
(44) Dines, A.; Ellis, M.; Blumberger, J. Stabilized Coupled Trajectory Mixed Quantum−Classical Algorithm with Improved Energy Conservation: CTMQC-EDI. *J. Chem. Phys.* **2023**, *159* (23), 234118.
(45) Pieroni, C.; Agostini, F. nonadiabatic Dynamics with Coupled Trajectories. *J. Chem. Theory Comput.* **2021**, *17* (10), 5969−5991.
(46) Arribas, E. V.; Vindel-Zandbergen, P.; Roy, S.; Maitra, N. T. Different Flavors of Exact-Factorization-Based Mixed Quantum-Classical Methods for Multistate Dynamics. *Phys. Chem. Chem. Phys.* **2023**, *25* (38), 26380−26395.
(47) Akimov, A. V.; Prezhdo, O. V. Second-Quantized Surface Hopping. *Phys. Rev. Lett.* **2014**, *113* (15), 153003.
(48) Dupuy, L.; Rikus, A.; Maitra, N. T. Exact-Factorization-Based Surface Hopping without Velocity Adjustment. *J. Phys. Chem. Lett.* **2024**, *15*, 2643−2649.
(49) Ha, J.-K.; Lee, I. S.; Min, S. K. Surface Hopping Dynamics beyond nonadiabatic Couplings for Quantum Coherence. *J. Phys. Chem. Lett.* **2018**, *9* (5), 1097−1104.
(50) Filatov, M.; Paolino, M.; Min, S. K.; Kim, K. S. Fulgides as Light-Driven Molecular Rotary Motors: Computational Design of a Prototype Compound. *J. Phys. Chem. Lett.* **2018**, *9* (17), 4995−5001.
(51) Ha, J.-K.; Min, S. K. Independent Trajectory Mixed Quantum-Classical Approaches Based on the Exact Factorization. *J. Chem. Phys.* **2022**, *156* (17), 174109.
(52) Shin, S.; Metiu, H. nonadiabatic Effects on the Charge Transfer Rate Constant: A Numerical Study of a Simple Model System. *J. Chem. Phys.* **1995**, *102* (23), 9285−9295.
(53) Engel, V.; Metiu, H. A Quantum Mechanical Study of Predissociation Dynamics of NaI Excited by a Femtosecond Laser Pulse. *J. Chem. Phys.* **1989**, *90* (11), 6116−6128.
(54) Vindel-Zandbergen, P.; Ibele, L. M.; Ha, J.-K.; Min, S. K.; Curchod, B. F. E.; Maitra, N. T. Study of the Decoherence Correction Derived from the Exact Factorization Approach for nonadiabatic Dynamics. *J. Chem. Theory Comput.* **2021**, *17* (7), 3852−3862.
(55) Filatov, M.; Min, S. K.; Choi, C. H. Theoretical Modelling of the Dynamics of Primary Photoprocess of Cyclopropanone. *Phys. Chem. Chem. Phys.* **2019**, *21* (5), 2489−2498.
(56) Akimov, A. V. Libra: An Open-Source "Methodology Discovery" Library for Quantum and Classical Dynamics Simulations. *J. Comput. Chem.* **2016**, *37* (17), 1626−1649.
(57) Shakiba, M.; Smith, B.; Li, W.; Dutra, M.; Jain, A.; Sun, X.; Garashchuk, S.; Akimov, A. Libra: A Modular Software Library for Quantum nonadiabatic Dynamics. *Softw. Impacts* **2022**, *14*, 100445.
(58) Akimov, A. V. Energy-Conserving and Thermally Corrected Neglect of Back-Reaction Approximation Method for nonadiabatic Molecular Dynamics. *J. Phys. Chem. Lett.* **2023**, *14* (51), 11673−11683.
(59) Temen, S.; Jain, A.; Akimov, A. V. Hierarchical Equations of Motion in the Libra Software Package. *Int. J. Quantum Chem.* **2020**, *120* (22), No. e26373.
(60) Dutra, M.; Garashchuk, S.; Akimov, A. V. The Quantum Trajectory-Guided Adaptive Gaussian Methodology in the Libra Software Package. *Int. J. Quantum Chem.* **2023**, *123* (8), No. e27078.
(61) Akimov, A. V. A Simple Phase Correction Makes a Big Difference in nonadiabatic Molecular Dynamics. *J. Phys. Chem. Lett.* **2018**, *9* (20), 6096−6102.
(62) Shakiba, M.; Akimov, A. V. Dependence of Electron−Hole Recombination Rates on Charge Carrier Concentration: A Case Study of nonadiabatic Molecular Dynamics in Graphitic Carbon Nitride Monolayers. *J. Phys. Chem. C* **2023**, *127* (19), 9083−9096.
(63) Shakiba, M.; Stippell, E.; Li, W.; Akimov, A. V. nonadiabatic Molecular Dynamics with Extended Density Functional Tight-Binding: Application to Nanocrystals and Periodic Solids. *J. Chem. Theory Comput.* **2022**, *18* (9), 5157−5180.
(64) Smith, B.; Shakiba, M.; Akimov, A. V. nonadiabatic Dynamics in Si and CdSe Nanoclusters: Many-Body vs Single-Particle Treatment of Excited States. *J. Chem. Theory Comput.* **2021**, *17* (2), 678−693.
(65) Smith, B.; Shakiba, M.; Akimov, A. V. Crystal Symmetry and Static Electron Correlation Greatly Accelerate Nonradiative Dynamics in Lead Halide Perovskites. *J. Phys. Chem. Lett.* **2021**, *12* (9), 2444−2453.
(66) Akimov, A. V. Extending the Time Scales of nonadiabatic Molecular Dynamics via Machine Learning in the Time Domain. *J. Phys. Chem. Lett.* **2021**, *12* (50), 12119−12128.
(67) Akimov, A. V. Excited State Dynamics in Monolayer Black Phosphorus Revisited: Accounting for Many-Body Effects. *J. Chem. Phys.* **2021**, *155* (13), 134106.
(68) Han, D.; Ha, J.-K.; Min, S. K. Real-Space and Real-Time Propagation for Correlated Electron−Nuclear Dynamics Based on Exact Factorization. *J. Chem. Theory Comput.* **2023**, *19* (8), 2186−2197.
(69) Abedi, A.; Maitra, N. T.; Gross, E. K. U. Correlated Electron-Nuclear Dynamics: Exact Factorization of the Molecular Wavefunction. *J. Chem. Phys.* **2012**, *137* (22), 22A530.
(70) Abedi, A.; Agostini, F.; Suzuki, Y.; Gross, E. K. U. Dynamical Steps That Bridge Piecewise Adiabatic Shapes in the Exact Time-Dependent Potential Energy Surface. *Phys. Rev. Lett.* **2013**, *110* (26), 263001.
(71) Agostini, F.; Abedi, A.; Suzuki, Y.; Min, S. K.; Maitra, N. T.; Gross, E. K. U. The Exact Forces on Classical Nuclei in Non-Adiabatic Charge Transfer. *J. Chem. Phys.* **2015**, *142* (8), No. 084303.
(72) Shakiba, M.; Akimov, A. V. Generalization of the Local diabatization Approach for Propagating Electronic Degrees of Freedom in nonadiabatic Dynamics. *Theor. Chem. Acc.* **2023**, *142* (8), 68.
(73) Granucci, G.; Persico, M.; Toniolo, A. Direct Semiclassical Simulation of Photochemical Processes with Semiempirical Wave Functions. *J. Chem. Phys.* **2001**, *114* (24), 10608−10615.
(74) Alonso, J. L.; Clemente-Gallardo, J.; Echenique-Robba, P.; Jover-Galtier, J. A. Comment on "Correlated Electron-Nuclear Dynamics: Exact Factorization of the Molecular Wavefunction" [J. Chem. Phys. 137, 22A530 (2012)]. *J. Chem. Phys.* **2013**, *139* (8), No. 087101.
(75) Abedi, A.; Maitra, N. T.; Gross, E. K. U. Response to "Comment on 'Correlated Electron-Nuclear Dynamics: Exact Factorization of the Molecular Wavefunction'" [J. Chem. Phys. 139, 087101 (2013)]. *J. Chem. Phys.* **2013**, *139* (8), No. 087102.
(76) Fernandez-Alberti, S.; Roitberg, A. E.; Nelson, T.; Tretiak, S. Identification of Unavoided Crossings in nonadiabatic Photoexcited Dynamics Involving Multiple Electronic States in Polyatomic Conjugated Molecules. *J. Chem. Phys.* **2012**, *137* (1), No. 014512.
(77) Nelson, T.; Fernandez-Alberti, S.; Roitberg, A. E.; Tretiak, S. Artifacts Due to Trivial Unavoided Crossings in the Modeling of Photoinduced Energy Transfer Dynamics in Extended Conjugated Molecules. *Chem. Phys. Lett.* **2013**, *590*, 208−213.
(78) Wang, L.; Prezhdo, O. V. A Simple Solution to the Trivial Crossing Problem in Surface Hopping. *J. Phys. Chem. Lett.* **2014**, *5* (4), 713−719.
(79) Meek, G. A.; Levine, B. G. Evaluation of the Time-Derivative Coupling for Accurate Electronic State Transition Probabilities from Numerical Simulations. *J. Phys. Chem. Lett.* **2014**, *5* (13), 2351−2356.
(80) Mai, S.; Marquetand, P.; González, L. nonadiabatic Dynamics: The SHARC Approach. *WIREs Comput. Mol. Sci.* **2018**, *8* (6), No. e1370.
(81) Zhou, Z.; Jin, Z.; Qiu, T.; Rappe, A. M.; Subotnik, J. E. A Robust and Unified Solution for Choosing the Phases of Adiabatic

States as a Function of Geometry: Extending Parallel Transport Concepts to the Cases of Trivial and Near-Trivial Crossings. *J. Chem. Theory Comput.* **2020**, *16* (2), 835−846.
(82) Shu, Y.; Truhlar, D. G. Decoherence and Its Role in Electronically nonadiabatic Dynamics. *J. Chem. Theory Comput.* **2023**, *19* (2), 380−395.
(83) Larsen, R. E.; Bedard-Hearn, M. J.; Schwartz, B. J. Exploring the Role of Decoherence in Condensed-Phase nonadiabatic Dynamics: A Comparison of Different Mixed Quantum/Classical Simulation Algorithms for the Excited Hydrated Electron. *J. Phys. Chem. B* **2006**, *110* (40), 20055−20066.
(84) Subotnik, J. E. Fewest-Switches Surface Hopping and Decoherence in Multiple Dimensions. *J. Phys. Chem. A* **2011**, *115* (44), 12083−12096.
(85) Kosloff, D.; Kosloff, R. A Fourier Method Solution for the Time Dependent Schrödinger Equation as a Tool in Molecular Dynamics. *J. Comput. Phys.* **1983**, *52* (1), 35−53.
(86) Hyeon-Deuk, K.; Prezhdo, O. V. Photoexcited Electron and Hole Dynamics in Semiconductor Quantum Dots: Phonon-Induced Relaxation, Dephasing, Multiple Exciton Generation and Recombination. *J. Phys.: Condens. Matter* **2012**, *24* (36), 363201.
(87) Akimov, A. V.; Prezhdo, O. V. The PYXAID Program for Non-Adiabatic Molecular Dynamics in Condensed Matter Systems. *J. Chem. Theory Comput.* **2013**, *9* (11), 4959−4972.
(88) Holstein, T. Studies of Polaron Motion: Part II. The "Small" Polaron. *Ann. Phys.* **1959**, *8* (3), 343−389.
(89) Esch, M. P.; Levine, B. G. An Accurate, Non-Empirical Method for Incorporating Decoherence into Ehrenfest Dynamics. *J. Chem. Phys.* **2021**, *155* (21), 214101.
(90) Gu, B.; Garashchuk, S. Quantum Dynamics with Gaussian Bases Defined by the Quantum Trajectories. *J. Phys. Chem. A* **2016**, *120* (19), 3023−3031.
(91) Schiff, J.; Poirier, B. Communication: Quantum Mechanics without Wavefunctions. *J. Chem. Phys.* **2012**, *136* (3), No. 031102.
(92) Fay, T. P.; Lindoy, L. P.; Manolopoulos, D. E. Electron Spin Relaxation in Radical Pairs: Beyond the Redfield Approximation. *J. Chem. Phys.* **2019**, *151* (15), 154117.

https://doi.org/10.1021/acs.jctc.4c00343
J. Chem. Theory Comput. 2024, 20, 5022−5042